Stiffness gradients facilitate ovipositor bending and spatial probing control in a parasitic wasp

U. Cerkvenik[1], J.L. van Leeuwen[1], A. Kovalev[2], S.N. Gorb[2], Y. Matsumura[2], S.W.S Gussekloo[1,*]

[1]Experimental Zoology Group, Wageningen University, Wageningen, Netherlands

[2]Zoological Institute: Functional Morphology and Biomechanics, Kiel University, Kiel, Germany

*corresponding author: sander.gussekloo@wur.nl

Author contributions:

Conceptualization: U.C, J.L.v.L. and S.W.S.G.; methodology: U.C., S.W.S.G., A.K., J.L.v.L., and S.N.G.; resources: J.L.v.L. and S.N.G.; execution of experiments: U.C., A.K. and Y.M.; formal analysis: U.C., S.W.S.G., J.L.v.L., and A.K.; software: U.C.; visualization of results: U.C., S.W.S.G. and J.L.v.L.; writing of the original draft: U.C., S.W.S.G.; funding acquisition: J.L.v.L.; review and editing: U.C., S.W.S.G., J.L.v.L., A.K., Y.M., and S.N.G.

Abstract

Many parasitic wasps use slender and steerable ovipositors to lay eggs in hosts hidden in substrates, but it is currently unknown how steering is achieved. The ovipositors generally consist of three longitudinally connected elements, one dorsal and two ventral valves that can slide along each other. For the parasitic wasp *Diachasmimorpha longicaudata*, it has been shown that protraction of the ventral valves causes incurving of the ventral valves towards the dorsal one, which results in a change in probing direction. We hypothesise that this shape change is due to differences in bending stiffness along the ovipositor. Alignment of the stiff tip of the dorsal valve with a more flexible ventral S-shaped region situated just behind the tip straightens this S-bend and results in upwards rotation of the ventral tip. We show that the S-shaped region of the ventral valves has a low bending stiffness because it contains soft materials such as resilin. In contrast, the large cross-sectional area of the dorsal valve tip area probably results in a high bending stiffness. Elsewhere, the dorsal valve is less stiff than the ventral valves. Our results support the hypothesis that the interaction between the stiff dorsal valve portion and the more flexible S-shaped region co-determine the configurational tip changes required for steering the ovipositor in any desired direction along curved paths in the substrate. This provides novel insights in the understanding of steering mechanisms of the hymenopteran ovipositor, and for the application in man-made probes.

1. Introduction

For many insects it is essential that they can locate and reach resources hidden in substrates. Examples are mosquitos searching for blood vessels (Choumet et al., 2012), hemipterans probing for plant vasculature (Pollard, 1973), and parasitic wasps finding host larvae living in fruits or wood (Leyva et al., 1991; Vincent and King, 1995). Although the drilling mechanism is relatively well understood, it is still uncertain how these animals steer their probes in the desired direction.

Female parasitic wasps use slender, needle-like ovipositors to search for hosts hidden in various substrates (Cook and Rasplus, 2003; Pennacchio and Strand, 2006; Vilhelmsen et al., 2001). At least some species can actively steer their ovipositors, sometimes in complex trajectories in a single insertion (Cerkvenik et al., 2017; Elias et al., 2012; Quicke et al., 1995). One of these species, the braconid wasp *Diachasmimorpha longicaudata* (**Fig 1A**), can explore a wide range of the substrate from a single puncture point in any direction with respect to its body orientation, and can achieve highly curved insertion trajectories (Cerkvenik et al., 2017). How this and other insects species accomplish such curvatures is not completely understood, but for *D. longicaudata* the insertion curvature clearly correlates with configurational changes of the ovipositor (Cerkvenik et al., 2017).

Like in most wasps, the ovipositor of *D. longicaudata* consists of multiple elements (valves)—one dorsal and two ventral valves (**Fig 1B,C**) (Quicke et al., 1994; Smith, 1970)—and has an asymmetric tip in dorsoventral direction. The ventral valve tips bear backward-facing serrations, while the dorsal valve tip has a prominent bulge. Additionally, the ovipositor is S-shaped proximal to the tip when the valves are aligned (**Fig 1B, Video S1**). The valves are interconnected with tongue-and-groove linkages (**Fig 1C, Video S1**) that allow for sliding, but prevent separation of the valves (Smith, 1969; Vincent and King, 1995). Generally, the valves slide back and forth during probing in stiff materials (Cerkvenik et al., 2017), which is thought to reduce the overall net pushing force on the ovipositor in the process and limits the risk of buckling (Vincent and King, 1995).

Kinematic analysis of probing behaviour of *D. longicaudata*, showed that insertion with predominant protrusion of the ventral valves leads to curved trajectories (**Video S2** (Cerkvenik et al., 2017)). When protracted, the ventral valves curve towards the dorsal side of the ovipositor (**Fig 1D,** (Cerkvenik et al., 2017)). The dorsal curving of the ventral valves upon protraction is also observed outside a substrate, which implies that it occurs without external forces and is thus initiated from within the ovipositor (**Video S3**). In contrast, the dorsal valve remains approximately straight when it is protracted inside a substrate (**Fig 1D**, **VideoS2**, (Cerkvenik et al., 2017)). Additional to the changes in the very tip of the ovipositor, protraction of either the dorsal or the ventral valves results in a straightening of the S-bend region just proximal of the tip (Cerkvenik et al., 2017).

Because all the muscles that operate the valves are located in the animal's abdomen (Fergusson, 1988; Quicke et al., 1994; Scudder, 1961), we expect that the shape and curvature changes of the ovipositor tip occur only due to longitudinal shifts of the valves with respect to one another. It is therefore likely that the valve structural and material properties play an important role in such configurational changes, although external forces may enhance the overall effect.

One possible mechanism of induced bending has been described for parasitoids of genera *Zaglyptogastra* and *Pristomerus* and relies on the differential sclerotization of the valves (**Fig 1E**; Quicke, 1991). These wasps have ovipositors characterized by a series of intermittent arches and nodes near the tip (El-Heneidy and Quicke, 1991; Rousse and Van Noort, 2015). The arches are regions of sclerotized cuticle and are presumably stiffer than the nodes in between (Quicke, 1991). When the valves are aligned at their tips, arches and nodes of the dorsal and ventral valves also align. Protraction of one of the valves aligns the arches with the nodes on the other valve. This causes bending of the ovipositor as the nodes in each of the valves conform to the shape of the arches of their adjacent valves (Quicke, 1991). This mechanism can lead to bending of up to 180°, but is considered to be unsuitable for piercing hard substrates, which implies that these wasps only exploit existing holes in the substrate to access their hosts (Quicke, 1991).

Based on the anatomical characteristics of the ovipositor in *D. longicaudata*, and specifically the S-shaped region and the bulge on the dorsal valve, it is plausible that these wasps rely on a steering mechanism similar to the one described above. In the case of *D. longicaudata*, we hypothesize that the thickened portion of the dorsal valve might act as a stiff region and the S-shaped region as a deformable soft region. The stiff region will probably be highly sclerotized, whereas the part undergoing deformations, such as the S-shaped region, is exposed to repetitive strains and we therefore expect it to be adapted to minimize potential damage. A good candidate for mitigating harmful effects of loading in insect cuticle is resilin, an elastic protein that can undergo considerable strains without damage (Weis-Fogh, 1960). Resilin is commonly found in highly deformable and high-load bearing structures such as jumping legs of locusts and fleas (Burrows et al., 2008; Rothschild and Schlein, 1975), wings of beetles and dragonflies (Appel et al., 2015; Haas et al., 2000), beetle tarsal setae (Peisker et al., 2013), and sound producing organs of cicadas (Bennet-Clark, 1997).

To determine if stiffness variations in the ovipositor of *D. longicaudata* are present, we measured the bending stiffness along its length with small scale three point bending tests. This measured bending stiffness is determined by the shape (structure) of the ovipositor and its material properties. The second moment of area along the ovipositor length, describing the structural bending stiffness, was obtained from histological cross-sections and high-resolution Synchrotron X-ray microtomographs. The material composition of the ovipositor was qualitatively determined with confocal laser scanning microscopy (CLSM), and estimated by dividing the bending stiffness by the cross-sectional area. This gave us insight in the distribution of bending stiffness along the ovipositor of *D. longicaudata* and confirmed that there is a

mechanism of flexible and stiff zones which can be aligned to induce flexion. This provides a better understanding of how steering of probes can be achieved, and how it contributes to the probing versatility of parasitic wasps and potentially other probing insects. In addition, these findings also indicate how steering without intrinsic motors can be achieved in man-made probes.

2. Materials and methods

Animals

Animals were taken from the breeding colony at the Experimental Zoology Group at Wageningen University. The rearing protocol was the same as described in (Cerkvenik et al., 2017). All animals were anaesthetized with CO_2 and then decapitated immediately prior to fixation or experimentation.

Structural properties

Histology

For histological sectioning, the abdomen with the intact ovipositor was dissected from the body and fixed with a mixture of 0.1M sodium cacodylate buffer (dimethylarsenic acid sodium salt trihydrate; Merck, Germany), 2% (weight/volume) paraformaldehyde (Merck, Germany), and 2.5% (volume/volume) glutaraldehyde (EMS, PA, USA) on ice (0°C) for 2.5 h. The sample was washed with the 0.1M cacodylate buffer twice at 0°C, dehydrated in a series of ethanol solutions of increasing concentration from 50% to 100%, and transferred to epoxy resin (epon; Embed-812 Embedding Kit, EMS, PA, USA) through a sequence of solutions: a mixture of ethanol and propylene oxide (PO), pure PO, a series of 3:1 and 1:1 mixtures of PO and epon, and finally pure epon. The samples in epon were put in moulds and left to harden overnight at 60–65°C.

Semi-thin sections of 1 µm and 2 µm thickness were cut using a Reichert Ultracut S ultramicrotome (Leica Microsystems GmbH, Germany) and stained with a mixture of 1% Toluidine blue (VWR, PA, USA) and 1% Borax (disodium tetraborate decahydrate; Merck, Germany) dissolved in distilled water. The sections were photographed with a Leica DFC 450 C camera (5 MP) mounted on a Leica DM6b microscope (Leica Microsystems) with 40x or 100x objective. The images were stored as tiff files for further analysis.

High-resolution µCT scan

We removed the ovipositor from a single collection-specimen of *D. longicaudata* obtained from the Naturalis Biodiversity Center (Leiden, Netherlands) and mounted it on a pin using beeswax such that it could rotate around its longitudinal axis.

We scanned ~600 µm of the distal part of the ovipositor in two consecutive scans with 30 µm overlap at the TOMCAT beamline X02DA of the Swiss Light Source (Paul Scherrer Institute, Switzerland) with a 14 keV monochromatic X-ray beam. Projection images were recorded over an angular range of 180° with an angular step of 0.1° with a PCO Edge 5.5 sCMOS camera (exposure time of 100 ms), using a 5 µm thick FEE Tb:LSO scintillator and an optical magnification of 40x, resulting in an effective pixel width of 162.5 nm at a propagation distance of 9 mm. The scans were reconstructed using the gridrec reconstruction algorithm (Marone and Stampanoni, 2012) in conjunction with propagation-based phase contrast (delta/beta ratio = 100) as described by Paganin *et al.* (2002).

Analysis of the cross-sections

Seg3D 2.2.1 (University of Utah; (CIBC, 2016)) was used for segmentation of the reconstructed CT slices and histological images. Manually adapted thresholds were applied to roughly isolate the exoskeleton from the background. Masks were further manually adjusted, converted to binary images, and rotated such that the dorsal valve was on top. Histological sections were aligned manually, while the µCT slices were rotated by the average angle (169.66° ± 3.68°) measured from 16 slices spread equally along the length of the dataset.

To obtain more accurate estimates of the second moment of area, we recalculated the cross-sections perpendicular to the central axis along the full length of the µCT scan. The points along the axis served as centres of rotation for freely rotating planes. The orientation where these planes had the minimal cross-sectional area of the 3D reconstructed structure was considered perpendicular to the longitudinal axis of the scanned ovipositor. To avoid merging of the segmented valves, we applied an erosion algorithm on the entire reconstruction before the determining the minimal cross-sections, and a dilation algorithm with the same parameters afterwards. This algorithm performed well and produced few artefacts that were omitted in further analysis (see results **Fig 8A**: points in dashed circles in the right graph).

The second moment of area, a measure for structural bending resistance, was calculated for bending in the dorsi-ventral direction (I_x), which is the main direction of bending during normal probing (Cerkvenik et al., 2017). We analysed both the whole ovipositor (all three valves together) and its individual valves. Because material properties of the ovipositor in radial direction are unknown, it was impossible to accurately determine the neutral bending plane of the ovipositor. Instead, we calculated a rough estimation of the second moment of area with respect to the plane of the centroid. The I_x was approximated using:

$$I_x = \sum_i^n y_i^2 A_{pix}, \qquad \text{(Eqn 1)}$$

where y is the distance of the pixels from the horizontal axis going through the centroid of the cross-section, A_{pix} is the area represented by an individual pixel, and n is the number of pixels constituting the relevant cross-sectional area

(complete ovipositor or individual valve). The data of the ventral valves were aligned along their axes using their clearly recognizable maxima in I_x and averaged to obtain a single curve representing both ventral valves. The mean ventral valve was aligned with the dorsal valve based on the location of the tip vertices.

Scaling

The histological and µCT datasets were combined to form a full-length dataset. To correct for size differences between ovipositors, we calculated two scaling factors based on a randomly chosen set of animals (n=33) from our breeding colony. The ovipositors were dissected in phosphate buffer (pH 7.5, (NaCl; 136.9 mM), potassium chloride (KCl; 2.7 mM), monopotassium phosphate (KH_2PO_4; 1.5 mM), and sodium hydrogen phosphate (Na_2HPO_4 x $2H_2O$; 8.1 mM) in deionized water.) to prevent desiccation, and were photographed using an Olympus DP50 camera (5 MP; Olympus, Japan) mounted on the Zeiss Stemi SV-11 stereomicroscope with a 1.6x objective (Zeiss, Germany). The length of the ovipositor, its tip length (distal point of the dorsal valve to the apex of its enlargement) and the ovipositor width at two tip lengths from its distal vertex were measured using analySIS FIVE software (Olympus, Japan). We correlated both these measures with the overall length of the ovipositor (**Fig 2A, B**). The slopes of the major axis regression lines were used to calculate the sample lengths based on their tip length. This allowed us to express the measurement locations (distances along each sample) as percentages of the sample length.

To compute the correction factor for calculating the second moment of area of differently sized samples, we assumed isometric scaling of the ovipositors and we considered the ovipositor to be a hollow cylinder, the dorsal valve as a hollow half-cylinder, and the ventral valves as hollow quarter-cylinders. Formulas for the calculation of the second moment of area of these shapes differ only in their constants which cancel each other when deriving the correction factor, so we present here only the derivation for hollow quarter-cylinders.

For a hollow quarter cylinder, the second moment of area with respect to its centroid (I_x) is calculated with (Gere, 2008):

$$I_x = \left(\frac{\pi}{16} - \frac{4}{9\pi}\right) * (r_1^4 - r_2^4), \qquad \text{(Eqn 2)}$$

where r_1 and r_2 are respectively the outer and the inner radius of the full-cylinder cross-section (**Fig 2C**). A correction factor (c_f) is obtained by taking the ratio of I_x of two differently sized hollow cylinders:

$$\frac{I_{x,i}}{I_{x,j}} = \frac{\left(\frac{\pi}{16} - \frac{4}{9\pi}\right) * \left(r_{1,i}^4 - r_{2,i}^4\right)}{\left(\frac{\pi}{16} - \frac{4}{9\pi}\right) * \left(r_{1,j}^4 - r_{2,j}^4\right)} = \frac{r_{1,i}^4 - r_{2,i}^4}{r_{1,j}^4 - r_{2,j}^4} = c_f. \qquad \text{(Eqn 3)}$$

For the ventral valves $r_1 = 2r_2$, which was estimated from the segmented histological sections. However, obtaining these values for all samples was not feasible. Instead, we used the relationships between ovipositor width and its length

and between the dorsal valve tip length and the ovipositor length (**Fig 2A, B**) to express the correction factor in terms of the sample dorsal valve tip length (l_t).

The ovipositor width ($2r_1$) vs. length (L) relationship can be written as:

$$r_1 = \frac{s_w}{2} L, \qquad \text{(Eqn 4)}$$

where s_w is the width scaling factor. Considering the relationship between the radii, we can write a similar equation for the inner radius:

$$r_2 = \frac{s_w}{4} L, \qquad \text{(Eqn 5)}$$

Additionally, the dorsal tip length (l_t) varies with the ovipositor length with tip scaling factor s_t:

$$l_t = s_l L \Rightarrow L = \frac{l_t}{s_l}. \qquad \text{(Eqn 6)}$$

Equation 3 can be rewritten by expressing the radii as their respective width scaling factors and sample lengths (i.e. combining with Eqn 4 and Eqn 5) and substituting the sample lengths using Eqn 6:

$$c_f = \frac{r_{1,i}^4 - r_{2,i}^4}{r_{1,j}^4 - r_{2,j}^4} = \frac{\left(\frac{s_w}{2} L_i\right)^4 - \left(\frac{s_w}{4} L_i\right)^4}{\left(\frac{s_w}{2} L_j\right)^4 - \left(\frac{s_w}{4} L_j\right)^4} = \frac{\left(\frac{s_w}{2}\right)^4 \left({L_i}^4 - \left(\frac{L_i}{2}\right)^4\right)}{\left(\frac{s_w}{2}\right)^4 \left({L_j}^4 - \left(\frac{L_j}{2}\right)^4\right)} =$$
$$= \frac{\left(\frac{l_{t,i}}{s_l}\right)^4 - \left(\frac{l_{t,i}}{2s_l}\right)^4}{\left(\frac{l_{t,j}}{s_l}\right)^4 - \left(\frac{l_{t,j}}{2s_l}\right)^4} = \frac{\left(\frac{1}{s_l}\right)^4 \left({l_{t,i}}^4 - \left(\frac{l_{t,i}}{2}\right)^4\right)}{\left(\frac{1}{s_l}\right)^4 \left({l_{t,j}}^4 - \left(\frac{l_{t,j}}{2}\right)^4\right)} = \frac{{l_{t,i}}^4 - \left(\frac{l_{t,i}}{2}\right)^4}{{l_{t,j}}^4 - \left(\frac{l_{t,j}}{2}\right)^4}. \qquad \text{(Eqn 7)}$$

Correction factors were calculated for each sample. Depending on the location of the measurement, c_f was either computed with respect to the histological or µCT data set. The second moment of area obtained from the µCT scans were multiplied with the correction factors when calculating the second moments of area of the samples and their effective moduli of elasticity.

Bending stiffness

For the bending tests, the sheaths surrounding the ovipositor were removed, and the ovipositors were cut close to their base at the abdomen. Subsequently, the ovipositors were kept submerged in physiological (Ringer's) insect buffer solution (Barbosa et al 2014) at all times to prevent desiccation and to minimise changes in the material properties of the cuticle. To avoid damage to the ovipositor, we manipulated the samples only at the side opposite to the one intended for measurements. In total, we sampled data from 23 individuals. In 10 cases, the ovipositor valves were separated by carefully sliding them off each other. In most samples, the stiffness of their distal part was measured, but five ovipositors were measured at their proximal part. The dissected ovipositors or individual valves were clamped into a custom-made

clamp that kept the samples horizontal and prevented them from twisting when mounted in the experimental setup (**Fig 2D**).

Experimental setup

The set-up (**Fig 3A**) was positioned on a vibration isolation table TS-150 (Table Stable, Zwilikon, Switzerland) to avoid external interference. It consisted of three parallel carbon steel razorblades (FA-10; Feather)—two on the bottom pointing up and one on the top pointing down. The bottom razorblades were glued in the centre of a square Petri dish, more than ten times the diameter of the ovipositor apart from each other (distances of 350.48 µm or 357.90 µm, averages obtained from multiple measurements under the microscope). The horizontal position of the top blade was located exactly in between them. The Petri dish was fixed onto a Hexapod micro-motion positioning system (Physik Instrumente, Karlsruhe, Germany) that allowed translations in all directions with sub-micrometre resolution. To prevent sample desiccation during measurements, the Petri dish was filled with physiological (Ringer's) buffer solution for insects (Barbosa et al 2014) which was degassed to avoid air bubbles forming on the sample surface.

The top razor was mounted onto a force transducer (FORT10g, dynamic range 10 g, resolution < 0.01 mN; World Precision Instruments) fixed on a clamp stand and connected to a PC via a MP100WSW data acquisition system (Biopac Systems Inc., Goleta, CA, USA). The measurements were recorded with AcqKnowledge 3.7.0 software (Biopac System Inc., Goleta, CA, USA). The force transducer was calibrated by hanging a mass of 1655.3 mg on the lever of the force transducer with the attached razorblade. Because the transducer behaved linearly within its dynamic range, a single weight was sufficient to calibrate it (**Fig S1**).

Using the micromanipulator, the sample was placed perpendicular to the longitudinal axis of the razors and parallel to the bottom of the Petri dish. The Petri dish with the two razor blades was moved upwards in at least four steps (deflections) of 10 µm with inter-step intervals of several seconds (variable in number). The bending was done at 4–6 locations along each tested sample, depending on its length and the location of the clamp. The most distal part of the ovipositor (tip), which measures approximately 200 µm, could not be measured because it was too short to fit between the razorblades in the experimental setup. The most distal measurement of each sample that could be obtained was within the S-shaped region. This S-shaped region spans over approximately 200 µm and could always be positioned accurately in between the bottom two razorblades. The reaction forces on the top razorblade during bending were continuously recorded at a sampling frequency of 200 Hz.

All three point bending tests were monitored with a camera (Basler piA1900-32g, Basler Vision Technologies, 2 MP and 5 fps) mounted on a stereomicroscope and controlled with StreamPix 5 (NorPix Inc.) software. Light was provided by a cold light source isolated from the anti-vibrational table. The recorded videos were used to determine the location of the measurements along the length of the samples and to monitor slippage of the samples on the razorblades. We did not observe any slippage of the samples off the razorblades, although it is possible that minute and limited slippage occurred during bending, which were undetectable due to the uniform geometry and the lack of landmarks along the length of the samples. Our results might therefore slightly underestimate the actual stiffness of the ovipositor and its parts.

Analysis of force data

Analysis of the signal-to-noise (S-N) ratio with AcqKnowledge 3.7.3 software showed low values in highly flexible regions of the ovipositor such as the dorsal valves and the S-shaped region of the ventral valves (**Fig 3B**). Low S-N recordings were filtered with an infinite impulse response (IIR) band-stop filter (frequency 50 Hz, Q=0.1) to remove electrical noise and improve curve fitting in further analyses. The application of the IIR filter did not affect the accuracy of the fits (**Fig 3B**).

Data was first manually divided into individual sections corresponding to individual deflections, such that the sections overlapped by 1 second. This allowed for accurate fitting of the step function to the data (see below). Based on the video recordings, we omitted all force recordings where the razorblades were not in contact with the sample throughout the deflection step. Second, to avoid the error in the computation of the force change between subsequent steps due to non-standardized duration of the deflection steps, the single step force data were fitted with a Heaviside function adjusted for the exponential force relaxation:

$$f(t) = H(t)\left(A\left(1 - e^{-\lambda t}\right) + B\right) + C, \qquad \text{(Eqn 8)}$$

where t is time, $H(t)$ is the Heaviside step function, A denotes the relaxation force value for each step, λ is the exponential decay factor of the force relaxation, B is the amplitude of the step response, and C is the total offset of the curve. The time constant ($\tau = \frac{1}{\lambda}$) of the exponential decay was used to calculate the force increase within each deflection step as the value at $t = 3\tau$, which corresponds to 95.02% value of the steady state of the force response.

Data was corrected for stiffness of the experimental setup, which was determined by pressing two perpendicular razor blades against each other with 1 µm steps and analysing the obtained data in the same manner as described above.

The forces and corrected deflections across consecutive steps were then fitted with an exponential decline function (**Fig 3C**):

$$F(d) = \alpha(1 - \beta e^{-\gamma d}), \quad \text{(Eqn 9)}$$

where $F(d)$ is the force, d is the deflection, $\alpha, \beta, and\ \gamma$, are coefficients describing the final amplitude, the initial offset, and the steepness of the curve, respectively.

To compare the data obtained in the bending experiments with the observed curvature in probing animals, we estimated the mid-plane curvature of the samples during bending tests using (Gere, 2008):

$$d(x) = \frac{F(x)}{48EI}(4x^3 - 3xL^2), \quad \text{(Eqn 10)}$$

where x is the distance along the beam from one of the lateral pins, $d(x)$ is the deflection of the sample, $F(x)$ is the force needed for that deflection, E is the Young's modulus of the sample, I is its second moment of area, and L is the distance between the outer pins used for three point bending (**Fig 4A**). The second derivative of equation 10 is a good approximation of the induced curvature of the mid-plane of the beam (κ_{mid}), when the deflections are small. To compare the curvature of structures with different diameters, dimensionless curvature can be used: $\kappa^*_{\mathrm{mid}} = \kappa_{\mathrm{mid}} * w_{\mathrm{s}}$, where w_{s} is the width of the sample in the bending direction. For small deflections (i.e. $\kappa^*_{\mathrm{mid}} \ll 1$), we can use the following formula to calculate κ^*_{mid} for a given deflection:

$$\kappa^*_{\mathrm{mid}} = d''^{(x)} * w_{\mathrm{s}} = \frac{F(x)x}{2EI} * w_{\mathrm{s}}. \quad \text{(Eqn 11)}$$

For $(x = \frac{L}{2})$ and using the effective bending stiffness estimated from the first full deflection step ($E_{\mathrm{eff}}\ I_{\mathrm{x}}$; see below) instead of EI, we obtain the following equation:

$$\kappa^*_{\mathrm{mid}} = \frac{F(d)L}{4E_{\mathrm{eff}}I_{\mathrm{x}}} * w_{\mathrm{s}}, \quad \text{(Eqn 12)}$$

where $F(d)$ is the force recorded in a given deflection step, namely 10 µm, 20 µm, or 30 µm. For whole ovipositors, w_{s} = 30 µm, for ventral valves w_{s} = 20 µm, and for dorsal valves w_{s} = 10 µm.

The maximum dimensionless curvature of the whole ovipositor during natural probing is 0.048 (Cerkvenik et al., 2017). This value was adjusted to the size of ventral and dorsal valves by multiplying it with the diameter ratios ventral valve/whole ovipositor and dorsal valve/whole ovipositor, respectively. The same valve diameters were used as above. The dimensionless curvature induced in the first full deflection in three point bending experiments was similar to the one observed during kinematic experiments, whereas the second and third full deflection step usually induced higher curvatures than found in nature (**Fig 4B–D;** Cerkvenik et al., 2017). The effective stiffness of the ovipositor and its valves were therefore estimated from the first full deflection step—that is, the deflection step after omitting the deflection where the razorblades were not in contact with the sample throughout the bending.

Derived effective modulus of elasticity

We obtained the bending stiffness (*EI*) of the ovipositor and the valves from the three point bend experiments from 23 specimens using the Euler-Bernoulli beam theory, which is valid for slender structures and small deflections. At all measured locations along the ovipositor or the valves, the distance between the outer razorblades in our experimental setup was more than ten times bigger than the diameter of the samples. The ovipositor sections with greater diameters such as the distal and proximal ends were not used in three point bending measurements. Additionally, deflections were small as we estimated the stiffness of the samples based on the first deflection step of the bending experiment only. We therefore assume that the application of the Euler-Bernoulli beam theory is valid and that the bending stiffness can be obtained using:

$$EI = \frac{FL^3}{48d}, \qquad \text{(Eqn 13)}$$

were d is the deflection, F the bending force, and L the distance between the outer two razor blades. Because the ovipositor mainly consists out of cuticle, a composite material consisting of polysaccharide filaments (chitin) embedded in a protein matrix with possible metal incorporation that varies spatially (Vincent, 2002; Vincent and Wegst, 2004), it is very hard to obtain a reliable value for the stiffness based on localised nano-indentation measurements, especially in the ovipositor which shows gradients in material composition along both its length and depth. Instead, we estimated an effective modulus of elasticity at each location along the ovipositor ($E_{\mathrm{eff}}(l)$) by dividing the bending stiffness at each location by the second moment of area at the same locations ($I_x(l)$) obtained from histological and µCT data. To adjust them for size they were multiplied by the correction factor (c_f; see above):

$$E_{\mathrm{eff}}(l) = \frac{F(l)\,L^3}{48\,d\,I_{\mathrm{x}}(l)\,c_{\mathrm{f}}}, \qquad \text{(Eqn 14)}$$

Finite element analysis

To assess the effects of clamping and of the pre-bent beam shape of the S-curve on our results, we used finite element (FE) simulations using Abaqus/CAE 2017 (Simulia, Dassault Systemes). Because this assessment does not require a complete description of geometrical and material valve properties, we simulated solid cylindrical beams. To reduce the computational time, we took advantage of the lateral symmetry of the bending simulation and longitudinally halved the model and assumed lateral symmetry in the cut plane. The beam was therefore modelled as a half cylinder (length 5 mm, radius 7.5 µm). Bending was simulated such that it closely resembled the experimental conditions; one end of the beam was clamped and the razorblades were modelled as rectangular pins with rounded corners (width and height 5 µm, depth 8 µm, **Fig 5A**). The pins were positioned perpendicular to the beam and parallel to each other—the bottom

two pins were 350 µm apart and the top one was in their middle. The middle pin was located on top of the beam, the outer two pins on its bottom side. One end of the beam and the top pin were fixed in all three dimensions, while the bottom two pins were only allowed to move upwards and rotate in the vertical plane that was cutting the beam in half. The pins were modelled as non-deformable rigid bodies, thus resembling steel razorblades of much higher stiffness than the ovipositor. Additionally, we assumed frictionless contact between the beam and the pins and only considered the normal forces. As in the experiment, the bottom two pins were pushed towards the top one in three 10 µm steps. The vertical reaction forces (i.e. those in the bending direction) in the pins and at the fixed end of the beam were extracted for each deflection.

To determine the effect of the mesh size on the model output, we performed multiple simulations where the mesh size was varied, while keeping all other parameters constant. The mesh grid size was varied between 0.5 µm and 2 µm in steps of 0.5 µm both along the length of the beam and its perimeter. In these simulations, the bending location was kept at 4 mm from the clamp, the stiffness of the beam (E) was 10 GPa, and its Poisson's ratio (ν) was 0.3. The mesh size has little effect on the simulation output and the mesh grid size of 1 µm was used in subsequent simulations (**Fig 6A**).

For the effect of clamping, we used homogeneous material properties with a Poisson's ratio (ν) of 0.3, while the Young's modulus (E) was varied and set at 0.1 GPa, 1 GPa, and 10 GPa. Both parameters are within the range of their estimated values for insect cuticle (Vincent and Wegst, 2004). The effect of the clamping was negligible on beams with E = 0.1 GPa (**Fig. 6B**) and therefore simulations on beams with E < 0.1 GPa were not performed

The clamp effect was estimated by bending the beam at several distances from its fixed end, namely 1 mm, 2 mm, 3 mm, and 4 mm from the clamp. Clamping has little effect on soft beams ($E \leq 1$ GPa), whereas at higher beam stiffnesses (E=10 GPa and presumably above), the recorded forces strongly increase with a decreased distance to the clamp (**Fig 6B**). If the force in the top pin differed for more than 5% compared to the measurements done at the location farthest away from the clamp, we considered the force measurements inaccurate. To obtain the distance from the clamped end at which this threshold is reached, we interpolated the data for 10 GPa beam using a cubic spline. The threshold distance was 1.87 mm (**Fig 6B**). We therefore omitted all data points that were done at distances ≤ 1.87 mm from the clamp from our experimental dataset.

To determine the effect of the S-shape near the tip of the ovipositor, we created a cylinder with a similar S-shape located 4 mm away from the clamped end (**Fig 5B**). The ovipositor geometry was estimated from the micrographs obtained with confocal laser scanning microscopy (n = 4, for details see below). The S-shaped FE model beam consisted of a proximal bend in dorsal direction of 10° from its longitudinal axis, followed by a 20° bend in the ventral direction, and a 10° bend in dorsal direction again. The bends were spaced 100 µm apart and were rounded (r = 150 µm) to avoid structural discontinuities and the associated stress accumulation. The beam was assigned an E = 10 GPa and ν = 0.3.

Estimation of longitudinal strain after straitening the S-bend

To get an estimation of the strains occurring in the S-bend as a result of straightening we estimated it as follows. During full straightening, the outer surfaces will have the same arc length as the neutral plane in the bend position. We can calculate the length of the neutral plane (l_n) as the arc length over the curve which is

$$l_n = \theta_n R_n \quad \text{(Eqn 15)}$$

with θ_n the arc, and R_n the radius of the curve describing the bend part of the ovipositor in the bend position. Using the same formula, we can calculate arc length of the curve describing the outside of the ovipositor in the curved position (l_o), which has the same angle and an R equal to R_n minus the radius of the ovipositor (r). Strain (ε) is defined as

$$\varepsilon = \frac{l_n - l_o}{l_o}. \quad \text{(Eqn 16)}$$

Because θ is equal for all conditions this can be rewritten as

$$\varepsilon = \frac{R_n - (R_n - r)}{(R_n - r)} = \frac{r}{(R_n - r)}. \quad \text{(Eqn 17)}$$

Based on manual fitting of an arc through three lateral photographs we obtained a value of: R_n = 222 µm, and r = 17.7 µm. which results in an estimated strain of about 0.09.

Confocal Laser Scanning Microscopy

The material composition of the ovipositor was qualitatively assessed by visualizing autofluorescence in a confocal laser scanning microscope (ZeissLSM 700, Zeiss) with a 10x and 20x objective lenses (Zeiss Plan-Apochromat; numerical apertures 0.45 and 0.8, respectively). We applied the method established by Michels and Gorb (2012), which provides reliable information on the presence of resilin in insect cuticles. The ovipositors were put on a glass slide, embedded in glycerin, and covered with a cover glass. The sample was left under the microscope for half an hour to stabilize in the medium before scanning. Zeiss Efficient Navigation (ZEN) software (Carl Zeiss MicroImaging GmbH) was used to record the autofluorescence and create maximum intensity overlay images. We used excitation lasers of 405, 488, 555, and 639 nm and recorded the Z-stacks of autofluorescence using a 420–480 nm band-pass filter and ≥490, ≥560, and ≥640 nm long-pass filters, respectively. Before every scan, the laser power and detector gain of each laser were manually adjusted in live view at the scanning speed that was also used for the acquisition of the final image. We first increased both parameters until observing pixel saturation. Afterwards, the two parameters were carefully reduced to obtain an image with minimal number of the saturated pixels, before taking the micrographs. In the final image, the fluorescence light emissions were assigned to blue, green, red (50% intensity), and red (50% intensity) channels, respectively, according to the colour code by Michels and Gorb (2012).

3. Results

Gross anatomy of the ovipositor

The ovipositor of *D. longicaudata* is a slender structure that connects to the musculoskeletal apparatus at its base (**Fig 7A**; (Fergusson, 1988)). The three valves it consists of form a cylindrical structure approximately circular in cross-section, which encloses the egg canal (**Fig 7B, C**). The unloaded shaft of the ovipositor is slightly curved, making it dorsally concave. An S-shaped region is present just proximal to the distinct ovipositor tip (**Fig 7A** (inset)**, Fig. 7C**). For most of its length, the dorsal valve is crescent-shaped in cross section, while the ventral valve cross-sections resemble a quarter of an ellipse (**Fig 7B, C**). The dorsal valve connects to each ventral valve with a tongue-and-groove linkage that is 'mushroom-shaped' in cross-section (**Fig 7B**).

The cross-sectional area of the ovipositor varies little along most of its length (similar to **Fig 7B2**), except for its base (**Fig 7B1**) and the morphologically distinct tip (**Fig 7B3–B5**). The base of the ovipositor is enlarged and polygonal in cross-section. While the dorsal valve base is approximately five times wider than most of the ovipositor shaft, the ventral valves are only slightly enlarged compared to their cross-sectional size along the shaft (**Fig 7B1**). At the tip, distal to the S-shaped region, the dorsal and ventral valves both possess a bulging area before tapering towards the vertex (i.e. the point furthest away from the base). Additionally, the cross-sectional area of the tapered tips changes shape towards the tip vertices. The bulge on the dorsal valve changes from rectangular to oval, while that of the ventral valves changes from approximately oval to approximately triangular (**Fig 7B4–B5**).

Structural properties

The second moment of area varied along the ovipositor length in accordance with the above described anatomy (**Fig 7A, Fig 7B, Fig 8A,** for full comparison and statistics see **Table S1**). The I_x of both the whole ovipositor ($I_{x,ov}$; grey data in **Fig 8A**) and the dorsal valve ($I_{x,dv}$; light blue data in **Fig 8A**) sharply decreased from the base to the shaft, varied little along the shaft, and sharply increased at the location of the bulge of the dorsal valve, which was followed by a steep decrease towards its vertex. To illustrate, at the base (at 6.9% of the ovipositor length (OL)), $I_{x,ov}$ was $12.8 * 10^4$ µm^4, which diminished to about one quarter of this value along the shaft (lowest values around $3.64 * 10^4$ µm^4 at 66% OL), and increased at the bulge on the ovipositor tip (highest value of $19.93 * 10^4$ µm^4 at 96.8% OL), before decreasing to 0 at the end of the tip. The extreme values for the dorsal valve ($I_{x,dv}$) occurred at comparable locations, showed a similar pattern, but were smaller ($4.51 * 10^4$ µm^4 at 6.9% OL, $0.14 * 10^4$ µm^4 at 68% OL, and $3.06 * 10^4$ µm^4 at 96.9% OL).

The I_x of the ventral valves ($I_{x,vv}$) varied little along their entire shafts and increased only at their tip (dark blue data in **Fig 8A**). The values ranged from $0.60 * 10^4$ µm^4 at 6.9% OL to $0.80 * 10^4$ µm^4 at 63.6% OL, and were with $1.61 * 10^4$ µm^4 highest at 96.7% OL. The dorsal valve was in the dorsoventral direction thinner than the ventral ones along most of their length, except for the base (<10.5% OL; **Fig 8A**, left) and the bulge on the tip (>96.6% OL; **Fig 8A**, right).

The contribution of the individual valves to the second moment of area of the complete ovipositor (i.e. when computed with respect to the centroid obtained from whole ovipositor cross-sections; see **Fig S3**) were considerably higher than the values given here, but showed a similar pattern. Here we show the data with respect to the centroid of the object of interest, because they link directly to the bending stiffness measured in the three point bending experiments discussed below.

Bending stiffness

Bending stiffness ($E_{eff}I_x$) along the length of different parts of 23 different ovipositors was obtained with three point bending experiments in which one end of the sample was clamped. We excluded values obtained close to the clamp (see Materials and methods) and some additional measurements because twisting of the samples occurred during the bending tests, which resulted in erroneous force estimates. Values for bending stiffness reported here (for full comparison and statistics see **Table S2**) were all determined for curvatures within the observed natural range (see Materials and methods).

The shaft (<93% OL) of individual ventral valves were stiffer than the dorsal one (compare dark and light blue points in **Fig 8B)**. The mean recorded stiffness of the shaft of the whole ovipositor ($15.72 * 10^{-11}$ Nm^2) was approximately 3.6 times higher than the mean shaft stiffness of the isolated ventral valves ($4.40 * 10^{-11}$ Nm^2) and more than 17 times higher than the mean stiffness of the shaft of the isolated dorsal valve ($0.9 * 10^{-11}$ Nm^2).

The stiffness of both the ovipositor and the ventral valves was significantly lower in the S-shaped region between 93 and 96% OL (**Table S2**). The mean recorded value in the S-shaped region for the whole ovipositors ($5.12 * 10^{-11}$ Nm^2) is approximately a third (30.8%) of the mean value of the shaft. Similarly, the stiffness of the S-shaped region of the isolated ventral valves ($1.57 * 10^{-11}$ Nm^2) is also approximately a third (28.0%) of the mean stiffness of their shafts. FE studies showed that an S-shape morphology compared to a straight beam resulted in only a 7% (-0.43 mN vs -0.46 mN) reduction in measured reaction forces in a three point bending experiment, indicating that the differences in stiffness between the shaft and S-bend region cannot be explained by the S-bend shape alone.

The variation in the dorsal valve data is high and we did not observe significant differences between the shaft and the S-shaped region ($0.90 * 10^{-11}$ Nm^2 vs $0.88 * 10^{-11}$ Nm^2, **Table S2**). This variation is caused at least partially by the limited accuracy of the force transducer (see Materials and methods).

Material properties

Effective moduli of elasticity

The bending stiffness measured in our experiments depends on the second moment of area and the material properties of the ovipositor and the valves. We were able to estimate the material properties of these structures and express them as the effective modulus of elasticity (E_{eff}) by dividing the bending stiffness by the second moment of area. The effective modulus of elasticity showed the same variation along the length of the ovipositor as seen for the bending stiffness (**Fig 8C**). The effective elasticity of the ovipositor, ventral, and dorsal valves is significantly lower in the S-shaped region than in the shaft (**Table S2**). For the whole ovipositor the effective modulus of elasticity of the S-shaped region is almost 4 times lower than the shaft (0.92 GPa vs 3.60 GPa), over 3 times lower in the ventral valves (1.46 GPa vs 4.81 GPa), and only 1.6 times lower in the dorsal valve (3.7 GPa vs 5.95 GPa).

Qualitative assessment of ovipositor material composition

To link the differences in effective modulus of elasticity to actual differences in material properties we analysed the autofluorescence of the ovipositor with CLSM (**Fig 9**, **Fig S4**). The green (488 nm excitation) and red (555 and 639 nm excitation) autofluorescence signals indicate that the cuticle of the ovipositor is well sclerotized. The more flexible S-shaped region of the ventral valves is clearly less well-sclerotized and shows high levels of resilin (blue channel; 405 nm excitation; **Fig 9A**). Other regions with high resilin content are the most lateral parts of the dorsal valve (**Fig 9C**) and the valve inner walls forming the egg canal (**Fig 9B, D**).

4. Discussion

Parasitic wasps, mosquitoes and hemipterans are capable of inserting probes into a variety of substrates, and even explore the substrate by steering their probes in a range of directions (Cerkvenik et al., 2017; Choumet et al., 2012; Leopold et al., 2003). Hitherto, very little was known about how these animals induce a shift of the probing direction. The kinematic analysis of ovipositor insertions in the parasitic wasp *D. longicaudata* indicates that the reciprocal sliding movements of its valves may be important for both insertion (Vincent and King, 1995) and steering (Cerkvenik et al., 2017). In *D. longicaudata*, the protraction of the ventral valves over the dorsal one induces a clear shape change in the ovipositor tip that leads to curved insertion trajectories (**Video S2**, (Cerkvenik et al., 2017)).

We hypothesise that the ovipositor of *D. longicaudata* employs the same principle of differentially sclerotized (and therefore differentially stiff) valves as suggested for the arched ovipositors of *Zaglyptogastra* sp. and *Pristomerus* sp. (Quicke, 1991). For this mechanism to work, both soft and very stiff regions must be present. Analysis of the bending stiffness of the *D. longicaudata* ovipositor as a whole indeed showed an approximately 67% lower bending stiffness in

the S-shaped region than in the rest of the shaft. This reduction in stiffness is mainly caused by a change in material properties (effective modulus of elasticity). Structural properties of the S-shaped region even counteract the drop in stiffness as can be seen from the increased second moment of area in that region (**Table S1**). The reduced stiffness can neither be explained by the curved morphology as this only results in a 7% decrease in stiffness compared to a straight morphology with the same material. That the S-shaped region is composed of softer materials than other regions along the ovipositor is substantiated by the CLSM images, which show a stronger fluorescence signal indicative for the presence of relatively soft resilin at that location.

The derived effective moduli of elasticity of the ovipositor and its valves in *D. longicaudata* (**Fig 8C, Table S2**) are in agreement with those previously reported for other wasp ovipositors and the intromittent organs of beetles, which range from 0.6 to 10 GPa (Kundanati and Gundiah, 2014; Matsumura et al., 2017; Vincent and King, 1995). The reported Young's modulus of resilin, which is present in the S-shaped region of the ovipositor in *D. longicaudata*, is approximately 1 MPa (Vincent and Wegst, 2004, Gosline et al., 2002)—this is much smaller than our derived stiffness estimates of the sclerotized cuticle. Thus, the decreased stiffness of the S-shaped region of the ovipositor is likely due to the presence of resilin in the ventral valves at that location. However, the effective elasticity of the samples reported in **Fig. 8C** and **Table S2** are presumably influenced (reduced) by the possible sliding of the valves along each other during the three point bending experiments or by possible minute slippage of the samples on the razorblades. The effect of sliding valves was, however, not estimated in this study.

Although areas of increased stiffness have not been directly measured, it can be assumed that the tip of the ovipositor is stiffer than the rest of the ovipositor. We observed a dramatic increase in second moment of area of the whole ovipositor at the location of the dorsal bulge, where the mean second moment of area was two times higher than in the shaft (**Table S1**, **Fig 7**, **Fig 8A**). Because the autofluorescence of the materials of the shaft and the tip did not differ, we can assume that material properties are the same, and that the twofold increase of second moment of area at the bulge results in a twofold increase in bending stiffness of the ovipositor. This is mainly due to the bulge in the dorsal valve, which has a six times higher second moment of area than the dorsal valve shaft. The slight thickening of the ventral valve at the same location only leads to a very small increase in second moment of area (**Table S1**).

According to the steering hypothesis described above, alignment of flexible and stiff areas should lead to configurational changes of the ovipositor distal end. In the ovipositor of *D. longicaudata*, this occurs when the S-shaped region of either the dorsal or the ventral valve aligns with the morphologically distinct tip of the opposite valve. The S-shaped region and the bulge area of the tip have approximately the same length (3% OL, **Fig 1B, 7A,C; Table S1**), which facilitates an accurate alignment. The movement of the valves occurs *via* a complex mechanism of chitin plates in

the abdomen (Eggs et al., 2018, Smith, 1970), the description of which is outside the present scope. An *in vivo* study of probing kinematics has shown that *D. longicaudata* can displace the valves over a distance of 200 µm (Cerkvenik et al., 2017), which is sufficient for aligning the valve tip with the S-shaped region of their neighbours. Below, we describe how the alignment of the different parts may lead to these configurational changes, and consequently to a change in probing direction. We consider two valve configurations: *i)* protraction of the ventral valves, and *ii)* protraction of the dorsal valve (**Fig 10**).

Protraction of the ventral valves moves them from their rest position (**Fig 10A**) forward, such that their less stiff S-shaped regions align with the stiff bulge of the dorsal valve tip (**Fig 10B**). At the same time, the dorsal S-shaped region aligns with the shaft of the ventral valves. Due to the difference in stiffness, the dorsal valve bulge straightens the S-shaped region of the ventral valves as observed by Cerkvenik et al. (2017) **(Video S2**). Similarly, the S-shaped region of the dorsal valve is presumably straightened by the shaft of the ventral valves (**Fig 8B, Table S2**). We expect that after straightening of the S-shaped region the natural angle between the S-shaped region and the tip region remains, which causes the dorsal curving of the ovipositor (**Fig 10A, B**; (Cerkvenik et al., 2017)). While probing in stiff substrates, the substrate reaction forces presumably prevent the bending of the long ovipositor shaft, but allow for the curving of the short tip. Additionally, the bevel shape of the ventral valve tips (**Fig 1**, **10B**) generates asymmetric substrate reaction forces that potentially enhance the curving of the tip during insertion of the ovipositor, and may explain the high curvatures observed during probing (Cerkvenik et al., 2017).

Although this pattern seems straightforward, it is difficult to predict what happens upon protraction of a single ventral valve. The resulting bending moments on the ovipositor tip would in this case be asymmetric and could lead to local twisting of the valves. However, this is hard to substantiate experimentally and is outside the scope of this paper.

Dorsal valve protraction aligns the relatively soft S-shaped region of the dorsal valve with the stiffer ventral valve tips, which also possess a small bulge near their tips (**Fig 1D, 8, Table S1**). This presumably straightens the S-shaped region of the dorsal valve. The ventral S-shaped region in this case aligns with the shaft of the dorsal valve, and also straightens out (**Fig 1D, Fig 10C**; (Cerkvenik et al., 2017)). The straightening of both S-shaped regions should lead to dorsal curving of the ovipositor tip as explained above. This does occur when the ovipositor is outside a substrate (**Video S3**) but was not observed during natural probing (**Video S2**, Cerkvenik et al., 2017). We hypothesise that substrate reaction forces acting on the bevelled dorsal valve tip counteract any dorsal bending moments originating from the straightening of the S-shaped regions. Protraction of the dorsal valve inside a substrate therefore results in an approximately straight path, but in dorsal curving of the tip outside the substrate. Because the forces acting on the bevel counteract the bending moments within the ovipositor, we expect that protracting the dorsal valve by more than its tip

length leads to ventral curving. However, such big protraction amplitudes seem to be outside the natural probing range (Cerkvenik et al., 2017).

In both ventral and dorsal valve protraction, the S-shaped region of the ovipositor undergoes continuous deformations and is subjected to repetitive strains of about 9% (see Materials and methods), which could lead to damage due to material failure. The strains are larger in the thicker and stiffer ventral valves, compared to the relatively thin and flexible dorsal valve. It is unlikely that the expected strains in the ventral valves induce damage to their outer walls, because of the presence of resilin (**Fig 9A**). Resilin is known for its high resilience (≥ 92%) and its high maximum strain of 1.9 (Gosline et al., 2002). Therefore, we expect that it will not be damaged during the probing with the anticipated strains. The presence of resilin presumably makes the sclerotized cuticle tougher and reduces the likelihood of damage (e.g. Haas et al., 2000).

Interestingly, resilin-containing regions were also found in the inner walls of the valves around the egg canal and in the lateral sides of the dorsal valve (**Fig 9B–D**). These softer central regions could facilitate the passage of 'oversized' eggs during egg laying process (Austin, 1983; Austin and Browning, 1981; Bronner, 1985; Fulton, 1932; Whiting, 1967). Additionally, having softer lateral sides could be important in the wasps capability of exploring the substrate in an approximately half ellipsoid without rotating its body (Cerkvenik et al., 2017), by facilitating lateral bending or twisting of the ovipositor.

Although the functional principles of ovipositor bending are similar among *D. longicaudata*, *Zaglyptogatra* sp. and *Pristomerus* sp., the implementation of the mechanism in *D. longicaudata* differs from the other two species. Whereas *Zaglyptogastra* and *Pristomerus* possess a series of stiff (arches) and flexible (nodes) ovipositor regions, the ovipositor of *D. longicaudata* has only a single flexible area near its tip. This difference might be linked to the fact that *D. longicaudata* probes in solid substrates, while *Zaglyptogastra* and *Pristomerus* cannot (Quicke, 1991).

D. longicaudata probes in solid substrates such as citrus fruits (Leyva et al., 1991). The modulus of elasticity of orange peels estimated for freshly harvested fruits ranges between 3.5 GPa and 4.3 GPa (Fidelibus et al., 2002). It is likely that fruits infested with fruit-fly larvae are softer, although the stiffness of such fruits is not known. Nevertheless, *D. longicaudata* is capable of puncturing artificial gels with the stiffness of at least 0.2 GPa (Cerkvenik et al., 2017). We argue that this is presumably facilitated by the low number of stiff and flexible regions in the ovipositors of *D. longicaudata*. Although the flexible S-shaped region in the ovipositor of *D. longicaudata* may still bend when axial loading is applied, small offsetting of the valves potentially strengthens this region without inducing strong ovipositor curvatures that would hinder puncturing. The low number of flexible and stiff nodes might come at a price as it is likely that the S-shaped ovipositors cannot bend as much as the arched ones. We therefore hypothesise that the ovipositor S-

shaped region is a morphological adaptation for probing and steering in solid substrates such as fruits that occurs in *D. longicaudata*. Interestingly, S-shaped ovipositors also occur in species closely related to *D. longicaudata* (Van Achterberg, 1999; Wharton et al., 2012), which might face similar functional demands during probing.

Here we show that the structural and material properties of the ovipositor vary across its individual elements. This, together with the kinematics of individual elements (Cerkvenik et al., 2017), leads to controlled shape changes of the probe tip and therefore offers a degree of control over spatial probing of the animal. The probing principles found in parasitic wasps can be presumably also applied to other insect probers including mosquitoes and hemipterans. These animals also explore a variety of substrates with multi-element probes (Gordon and Lumsden, 1939; Pollard, 1973) that are moved reciprocally during substrate exploration (Choumet et al., 2012; Pollard, 1970). This kinematics indicates that these insects use similar principles of buckling avoidance and steering as described for parasitic wasps. It would be interesting to see if similar steering mechanism as described here can be also found in other insect groups. This would add to our understanding of the convergent evolution that led to the widespread usage of slender, multi-element probes capable of independent and reciprocal element movements and steering. Furthermore, it also indicates that such probes are highly effective for substrate exploration and studying their working principles may be also beneficial for the design of slender man-made probes.

Slender, multi-element probes inspired by parasitic wasp ovipositors have been developed and can be steered without placing actuators inside the probe and without axial rotation (Ko et al., 2010; Scali et al., 2017). The individual elements of such probes slide along each other and therefore form an adjustable bevel tip (Ko et al., 2011; Scali et al., 2017). The probe is steered by taking advantage of the substrate reaction forces acting on the adjustable bevel. Consequently, the amount of curving in such probes heavily depends on the material properties of the substrate and the probe. The steering mechanism described here is not dependent on the substrate interaction, although it can be enhanced by it. Therefore, application of a mechanism using stiff and deformable regions as described here will presumably result in probes less susceptible to substrate differences. The steering mechanism can be implemented by adjusting either the material properties or the cross-sectional area of the probe S-shaped region which would not compromise the diameter of the probe. Such design would therefore propel further miniaturization of man-made probes.

Acknowledgements

We acknowledge the Paul Scherrer Institut, Villigen, Switzerland for provision of synchrotron radiation beam time at the TOMCAT beamline X02DA of the SLS and would like to thank Chirstian Schlepuetz for invaluable assistance. We thank the Naturalis Biodiversity Center (RMNH; Leiden, Netherlands) and collection manager Frederique Bakker for help and providing the specimen used for CT-scanning. We also acknowledge the National Institute of General Medical Sciences of the National Institutes of Health for their role in the development of the Seg3D software (grant number P41 GM103545-18) for segmentation purposes. We thank Henk Schipper and Frank van den Berg for their help with histological sections of the ovipositor; Karen Leon-Kloosterziel for technical support, animal care, and help with ovipositor scaling analysis; and the user committee of the Netherlands Organization for Scientific Research Division Applied and Engineering Sciences (NWO TTW/NWO AES) WASP project and the members of the research group for their useful discussions.

Competing interests

The authors declare no competing interests.

Funding

This work was supported by NWO domain applied and engineering sciences (NWO TTW/NWO AES), grant 12712. The funders had no role in study design, data collection and analysis, or preparation of the manuscript. The user committee of the project agreed with the submission of this study.

Data availability

The data will be available on Dryad upon publication.

References

Appel, E., Heepe, L., Lin, C. P. and Gorb, S. N. (2015). Ultrastructure of dragonfly wing veins: Composite structure of fibrous material supplemented by resilin. *J. Anat.* **227**, 561–582.

Austin, A. D. (1983). Morphology and mechanics of the ovipositor system of *Ceratobaeus* Ashmead (Hymenoptera: Scelionidae) and related genera. *Int. J. Insect Morphol. Embryol.* **12**, 139–155.

Austin, A. D. and Browning, T. O. (1981). A mechanism for movement of eggs along insect ovipositors. *Int. J. Insect Morphol. Embryol.* **10**, 93–108.

Barbosa, P., Berry, D., and Kary, C. (2014) *Insect Histology: Practical Laboratory Techniques*. Chichester: John Wiley & Sons, Ltd.

Bennet-Clark, H. (1997). Tymbal mechanics and the control of song frequency in the cicada *Cyclochila australasiae*. *J. Exp. Biol.* **200**, 1681–1694.

Bronner, R. (1985). Anatomy of the ovipositor and oviposition behavior of the gall wasp *Diplolepis rosae* (Hymenoptera: Cynipidae). *Can. Ent.* **117**, 849–858.

Burrows, M., Shaw, S. R. and Sutton, G. P. (2008). Resilin and chitinous cuticle form a composite structure for energy storage in jumping by froghopper insects. *BMC Biol.* **6**, 41.

Cerkvenik, U., Van de Straat, B., Gussekloo, S. W. S. and van Leeuwen, J. L. (2017). The mechanisms of ovipositor insertion and steering of a parasitic wasp. *Proc. Natl. Acad. Sci. USA.* **114 (37)**, E7822–E7831.

Choumet, V., Attout, T., Chartier, L., Khun, H., Sautereau, J., Robbe-Vincent, A., Brey, P., Huerre, M. and Bain, O. (2012). Visualizing non infectious and infectious *Anopheles gambiae* blood feedings in naive and saliva-immunized mice. *PLoS One* **7**, e50464.

CIBC (2016). Seg3D: Volumetric Image Segmentation and Visualization. Scientific Computing and Imaging Institute (SCI), Download from: http://www.seg3d.org.

Cook, J. M. and Rasplus, J.-Y. (2003). Mutualists with attitude: coevolving fig wasps and figs. *Trends Ecol. Evol.* **18**, 241–248.

Eggs, B., Birkhold, A. I., Röhrle, O. and Betz, O. (2018). Structure and function of the musculoskeletal ovipositor system of an ichneumonid wasp. *BMC Zoology*, **3**, 1–25.

El-Heneidy, A. H. and Quicke, D. L. J. (1991). The Indo-Australian species of the braconine wasp genus Zaglyptogastra Ashmead. *J. Nat. Hist.* **25**, 183–201.

Elias, L. G., Teixeira, S. P., Kjellberg, F. and Santinelo Pereira, R. A. (2012). Diversification in the use of resources by *Idarnes* species: bypassing functional constraints in the fig-fig wasp interaction. *Biol. J. Linn. Soc.* **106**, 114–122.

Fergusson, N. D. M. (1988). A comparative study of the structures of phylogenetic importance of female genitalia of the Cynipoidea (Hymenoptera). *Syst. Entomol.* **13**, 13–30.

Fidelibus, M. W., Teixeira, A. A. and Davies, F. S. (2002). Mechanical properties of orange peel and fruit treated pre-harvest with gibberellic acid. *Trans. Am. Soc. Agric. Eng.* **45**, 1057–1062.

Fulton, B. B. (1932). Notes on *Habrocytus cerealellae*, parasite of the Angoumois grain moth. *Ann. Entomol. Soc. Am.* **26**, 536–553.

Gere, J. M. (2008) *Mechanics of Materials. 6th edn*. Belmont CA, Brooks/Cole–Thomson Learning, Inc.

Gordon, R. M. and Lumsden, W. H. R. (1939). A study of the behaviour of the mouth-parts of mosquitoes when taking up blood from living tissue together with some observations on the ingestion of microfiliarie. *Ann. Trop. Med. Parasitol.* **33**, 259–278.

Gosline, J., Lillie, M., Carrington, E., Guerette, P., Ortlepp, C. and Savage, K. (2002). Elastic proteins: Biological roles and mechanical properties. *Philos. Trans. R. Soc. B Biol. Sci.* **357**, 121–132.

Haas, F., Gorb, S. and Blickhan, R. (2000). The function of resilin in beetle wings. *Proc. R. Soc. B Biol. Sci.* **267**, 1375–1381.

Ko, S. Y., Davies, B. L. and Rodriguez y Baena, F. (2010). Two-dimensional needle steering with a "programmable bevel" inspired by nature: Modeling preliminaries. *Intell. Robot. Syst. (IROS), 2010 IEEE/RSJ Int. Conf.* 2319–2324.

Ko, S. Y., Frasson, L. and Rodriguez y Baena, F. (2011). Closed-loop planar motion control of a steerable probe with a "programmable bevel" inspired by nature. *IEEE Trans. Robot.* **27**, 970–983.

Kundanati, L. and Gundiah, N. (2014). Biomechanics of substrate boring by fig wasps. *J. Exp. Biol.* **217**, 1946–1954.

Leopold, R. A., Freeman, T. P., Buckner, J. S. and Nelson, D. R. (2003). Mouthpart morphology and stylet penetration of host plants by the glassy-winged sharpshooter, *Homalodisca coagulata*, (Homoptera: Cicadellidae). *Arthropod Struct. Dev.* **32**, 189–199.

Leyva, J. L., Browning, H. W. and Gilstrap, F. E. (1991). Effect of host fruit species, size, and color on parasitization of *Anastrepha ludens* (Diptera: Tephritidae) by *Diachasmimorpha longicaudata* (Hymenoptera: Braconidae). *Environ. Entomol.* **20**, 1469–1474.

Marone, F. and Stampanoni, M. (2012). Regridding reconstruction algorithm for real-time tomographic imaging. *J. Synchrotron Radiat.* **19**, 1029–1037.

Matsumura, Y., Kovalev, A. E. and Gorb, S. N. (2017). Penetration mechanics of a beetle intromittent organ with bending stiffness gradient and a soft tip. *Sci. Adv.* **3**, eaao5469.

Michels, J. and Gorb, S. N. (2012). Detailed three-dimensional visualization of resilin in the exoskeleton of arthropods using confocal laser scanning microscopy. *J. Microsc.* **245**, 1–16.

Paganin, D., Mayo, S. C., Gureyev, T. E., Miller, P. R. and Wilkins, S. W. (2002). Simultaneous phase and amplitude extraction from a single defocused image of a homogeneous object. *J. Microsc.* **206**, 33–40.

Peisker, H., Michels, J. and Gorb, S. N. (2013). Evidence for a material gradient in the adhesive tarsal setae of the ladybird beetle *Coccinella septempunctata*. *Nat. Commun.* **4**, 1607–1608.

Pennacchio, F. and Strand, M. R. (2006). Evolution of developmental strategies in parasitic Hymenoptera. *Annu. Rev. Entomol.* **51**, 233–258.

Pollard, D. G. (1970). The mechanism of stylet movement in *Psylla mali* Schmidberger (Homoptera: Psyllidae). *Zool. J. Linn. Soc.* **49**, 295–307.

Pollard, D. G. (1973). Plant penetration by feeding aphids (Hemiptera, Aphidoidea): a review. *Bull. Entomol. Res.* **62**, 631.

Quicke, D. L. J. (1991). Ovipositor mechanics of the braconine wasp genus *Zaglyptogastra* and the ichneumonid genus *Pristomerus*. *J. Nat. Hist.* **25**, 971–977.

Quicke, D. L. J., Fitton, M. G., Tunstead, J. R., Ingram, S. N. and Gaitens, P. V. (1994). Ovipositor structure and relationships within the Hymenoptera, with special reference to the Ichneumonoidea. *J. Nat. Hist.* **28**, 635–682.

Quicke, D. L. J., Fitton, M. and Harris, J. (1995). Ovipositor steering mechanisms in braconid wasps. *J. Hymenopt. Res.* **4**, 110–120.

Rothschild, M. and Schlein, J. (1975). The jumping mechanism of *Xenopsylla cheops* I. Exoskeletal structures and musculature. *Philos. Trans. R. Soc. Lond. B. Biol. Sci.* **271**, 457–490.

Rousse, P. and Van Noort, S. (2015). Revision of the Afrotropical species of *Pristomerus* (Ichneumonidae: Cremastinae), with descriptions of 31 new species. *Eur. J. Taxon.* 1–129.

Scali, M., Pusch, T., Breedveld, P. and Dodou, D. (2017). Ovipositor-inspired steerable needle: design and preliminary experimental evaluation. *Bioinspir. Biomim.* **13**, 016006.

Scudder, G. G. E. (1961). The comparative morphology of the insect ovipositor. *Trans. R. Entomol. Soc. London* **113**, 2–40.

Smith, E. L. (1969). Evolutionary morphology of external insect genitalia. 1. Origin and relationships to other appendages. *Ann. Entomol. Soc. Am.* **62**, 1051–1079.

Smith, E. L. (1970). Evolutionary morphology of the external insect genitalia. 2. Hymenoptera. *Ann. Entomol. Soc. Am.* **63**, 1–27.

Van Achterberg, C. (1999). The Palaearctic species of the genus *Diachasmimorpha* Viereck (Hymenoptera: Braconidae: Opiinae). *Zool. Meded.* **73**, 1–10.

Vilhelmsen, L., Isidoro, N., Romani, R., Basibuyuk, H. H. and Quicke, D. L. J. (2001). Host location and oviposition in a basal group of parasitic wasps: the subgenual organ, ovipositor apparatus and associated structures in the Orussidae (Hymenoptera, Insecta). *Zoomorphology* **121**, 63–84.

Vincent, J. F. V (2002). Arthropod cuticle: a natural composite shell system. *Compos. Part A Appl. Sci. Manuf.* **33**, 1311–

1315.

Vincent, J. F. V. and King, M. J. (1995). The mechanism of drilling by wood wasp ovipositors. *Biomimetics* **3**, 187–201.

Vincent, J. F. V. and Wegst, U. G. K. (2004). Design and mechanical properties of insect cuticle. *Arthropod Struct. Dev.* **33**, 187–199.

Weis-Fogh, T. (1960). A rubber-like protein in insect cuticle. *J. Exp. Biol.* **37**, 889–907.

Wharton, R., Ward, L. and Miko, I. (2012). New neotropical species of Opiinae (Hymenoptera, Braconidae) reared from fruit-infesting and leafmining Tephritidae (Diptera) with comments on the *Diachasmimorpha mexicana* species group and the genera *Lorenzopius* and *Tubiformopius*. *Zookeys* **243**, 27–82.

Whiting, A. R. (1967). The biology of the parasitic wasp *Mormoniella vitripennis* (= *Nasonia Brevicornis*) (Walker). *Q. Rev. Biol.* **42**, 334–406.

Figures

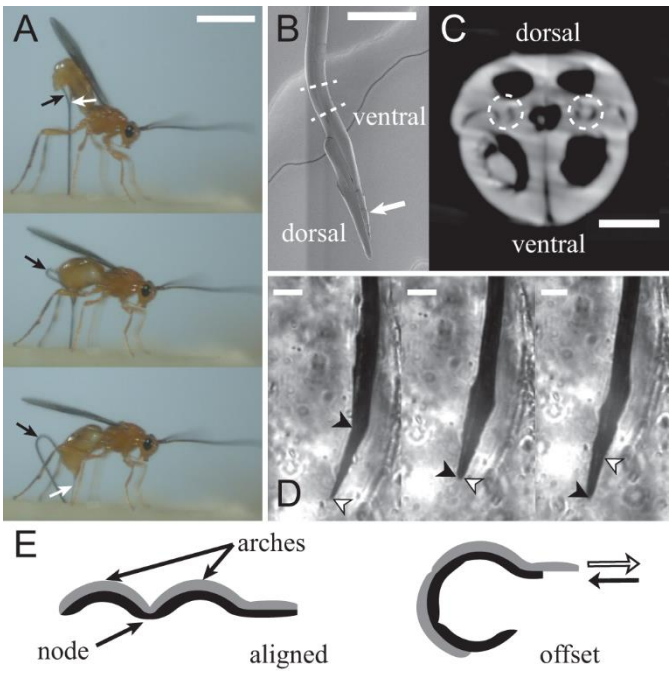

Fig 1. Wasps ovipositor morphology and kinematics. A) Ovipositor insertion by *D. longicaudata*. Top: the ovipositor (white arrow) is positioned vertically while supported by the sheaths (black arrow) before insertion. Middle: during insertion, the sheaths peel away from the ovipositor at its base. Bottom: at full insertion the sheaths completely detach. Scale bar 5 mm. **B)** SEM image of the ovipositor tip—side view; white arrow indicates serrations on the ventral valves. dashed lines indicate the position of the cross section shown in C. Scale bar 100 µm. **C)** Ovipositor cross-section (see B) showing the dorsal valve (top) and two ventral valves (bottom), dashed circles indicate the tongue-and-groove connection. Scale bar 10 µm. **D)** Ventral valves (white arrow heads) curve towards the dorsal valve (black arrow heads) upon protraction. No such curving is observed when the dorsal valve is protracted. Scale bar 50 µm. **E)** Proposed bending principle in ovipositors with differential valve sclerotization (Quicke, 1991). Left: when the highly sclerotized and therefore stiff arches align the ovipositor is characteristically arched and 'straight' at a larger spatial scale. Right: Upon protraction of the ventral valves the arches align with the less sclerotized softer nodal regions and the ovipositor bends. A–D modified from Cerkvenik et al., 2017.

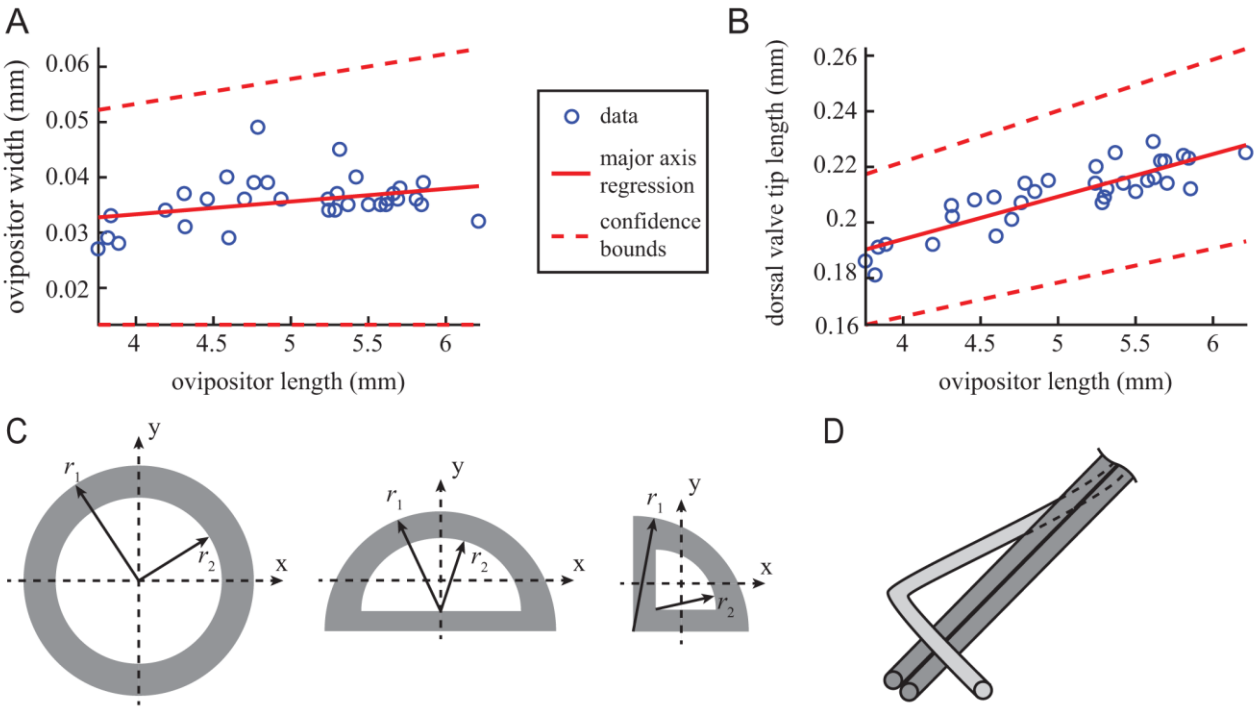

Fig 2. Length of the morphologically distinct tip and the width of the ovipositor scale with its length. Data were obtained from 33 animals. **A)** The ovipositor diameter increases with ovipositor length. **B)** The length of the dorsal valve tip increases with ovipositor length. **C)** Simplified cross-sectional geometry used to determine the scaling factors. The cross-section of the ovipositor was modelled as a hollow cylinder, the dorsal valve that of a hollow half cylinder, and the ventral valve that of a hollow quarter cylinder. The lumina of the valves were assumed to have the same shape as the valves themselves. The radii of the outer shape and the lumina are denoted with r_1 and r_2, respectively. Intersection of dashed lines indicate the origin of the coordinate system used to calculate the second moment of area of the depicted structure. **D)** Schematics of the holder made out of three insect pins used to clamp the samples during three point bending tests. Two straight pins were glued together. The third pin was bent in an L-shape; its straight end was glued to the other two pins, whereas its L-shaped end was twisted around the straight pins. The samples were fixed between the straight pins and the L-shaped pin.

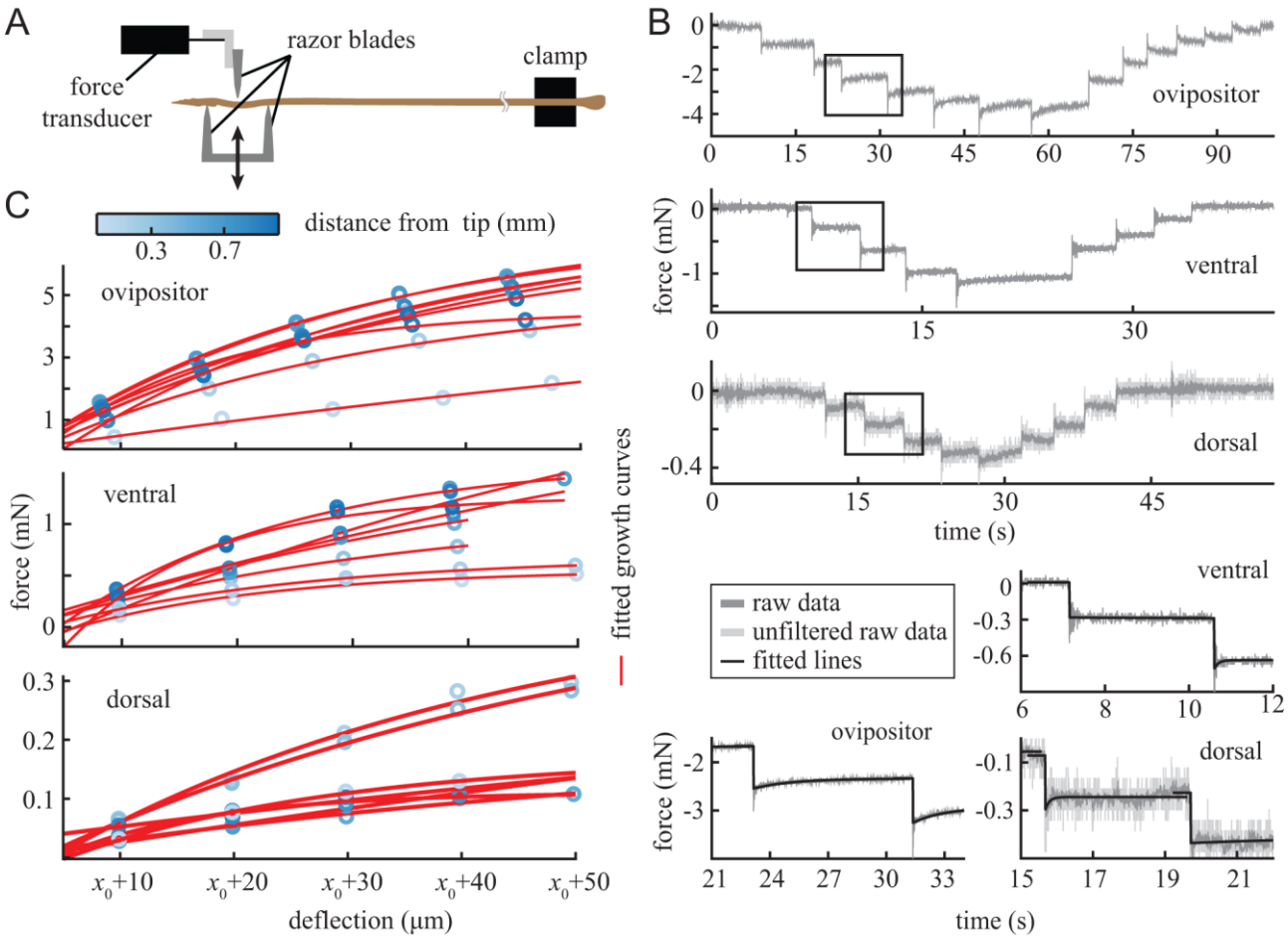

Fig 3. Three point bending experiments along the ovipositor, ventral valve, and dorsal valve. A) Schematics of the experimental setup. Samples were clamped at one end and positioned between three razorblades. Bending was achieved by pushing the bottom two razorblades towards the top one, which was connected to a force transducer. **B)** Example data of force recordings for the entire ovipositor (all three elements together) and individual ventral and dorsal valves. Data used in the analysis are shown in black. These recordings contained electrical noise (i.e. light grey line) and were therefore filtered with a band stop IIR filter (50Hz, Q=0.1) which reduced the noise before subsequent analysis. Increase in absolute value of the force during bending was calculated from curves fitted to individual deflections steps (bottom three graphs). **C)** Example data of force vs. deflection for all three types of samples. We did not control for the distance between the sample and the top razor at the start of the bending. Therefore, the measurements differ in the amplitude of the initial deflection step (x_0). The colour intensity of the blue symbols denotes location of bending along the sample length—darkness increases with distance from the tip. The data were fitted with an exponential decay function (increasing form) growth curve (red lines). The slope of the curve at the first recorded point was used to calculate the sample $E_{\text{eff}} I_x$.

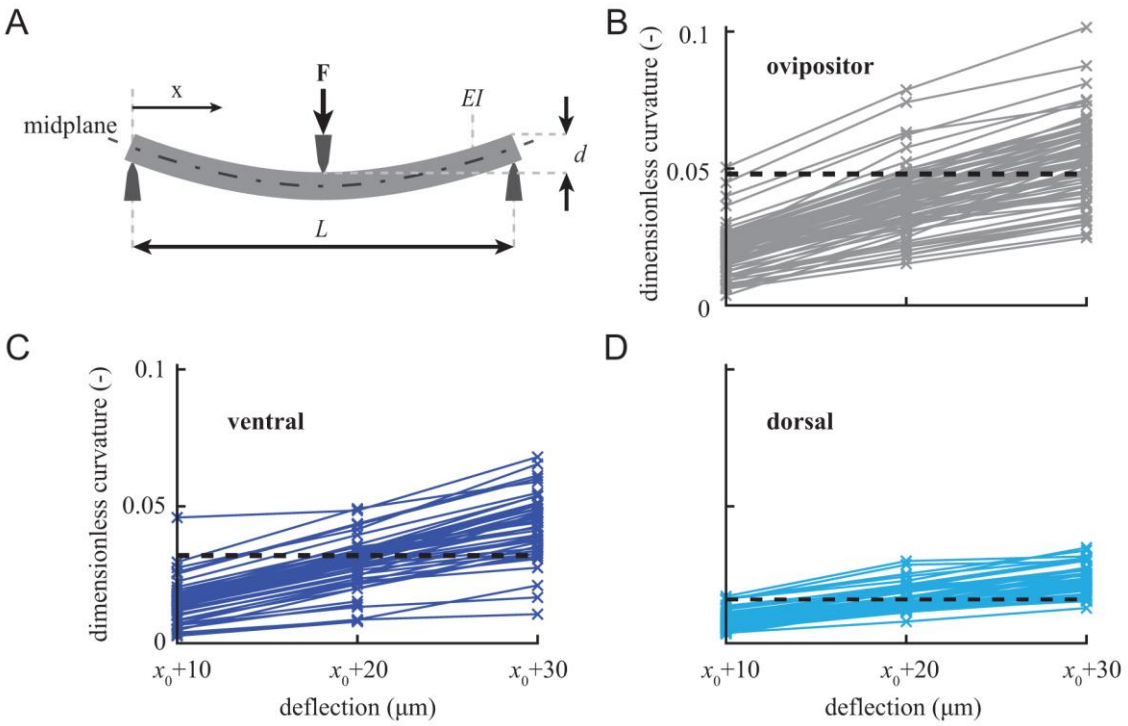

Fig 4. Samples were during experiments bent in their natural range with extension. A) Schematics of three point bending experiment with parameters used for estimating the curvature during bending from the recorded force. We estimated the mid-plane curvature of the sample assuming central loading. The estimated dimensionless curvature for the whole ovipositor (**B**), ventral (**C**), and dorsal valves (**D**) at each tested location along their length. The maximal dimensionless curvature observed in kinematic experiments is indicated with a horizontal black dashed line. The dimensionless curvature of the whole ovipositor (0.048) was taken from Cerkvenik et al. (2017) and adjusted for the diameters of individual valves. In the first full deflection step, one whole ovipositor sample, one ventral valve sample, and two dorsal valve samples slightly exceeded the maximal values recorded *in vivo*. In the second deflection step, seven whole ovipositors and approximately half of the single ventral and dorsal valves exceeded the natural range. In the third deflection step, more than half of the samples exceeded their natural bending range.

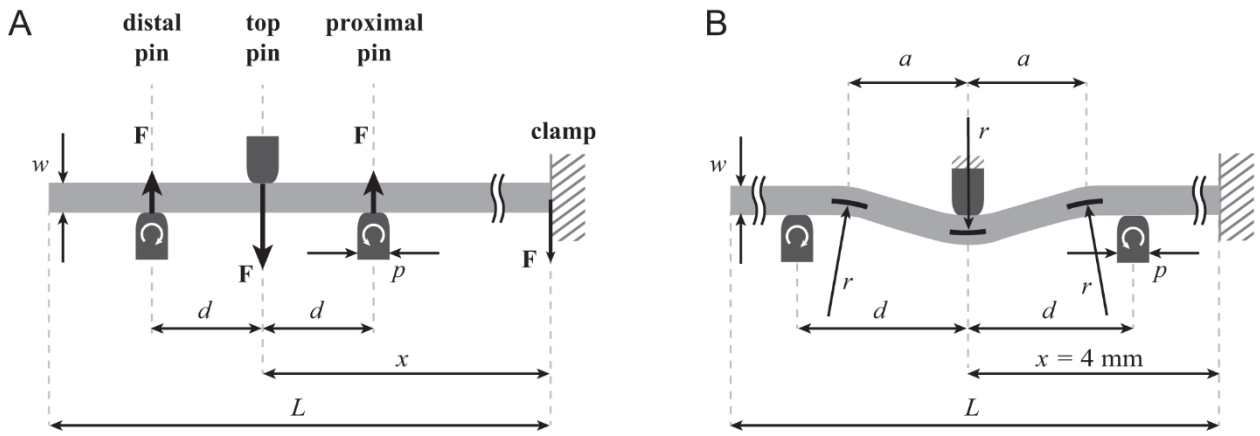

Fig 5. FEM simulations of three point bending tests on cantilever beams. A) Schematics of the FEM model. The cantilever beam of width w = 15 µm and length L = 5 mm was bent between three rectangular pins with rounded corners of width p = 5 µm. The distance between the bottom two pins was 350 µm (= 2d) and the top pin was positioned in their middle. The pins were modelled as rigid bodies. The top pin was fixed in all directions and the bottom two pins were allowed to rotate in plane indicated in the schematics (white arrows). Bending was done at four different distances from the clamp (x) and the vertical reaction forces (**F**) in the pins and at the fixed end of the cantilever were computed. **B)** Schematics of model used to determine the effect of the bent beam geometry. The symbols are same as in (A), except for a = 100 µm and r = 150 µm which denote the length of the curved region and maximal local radius of curvature in the curve (short, black lines), respectively.

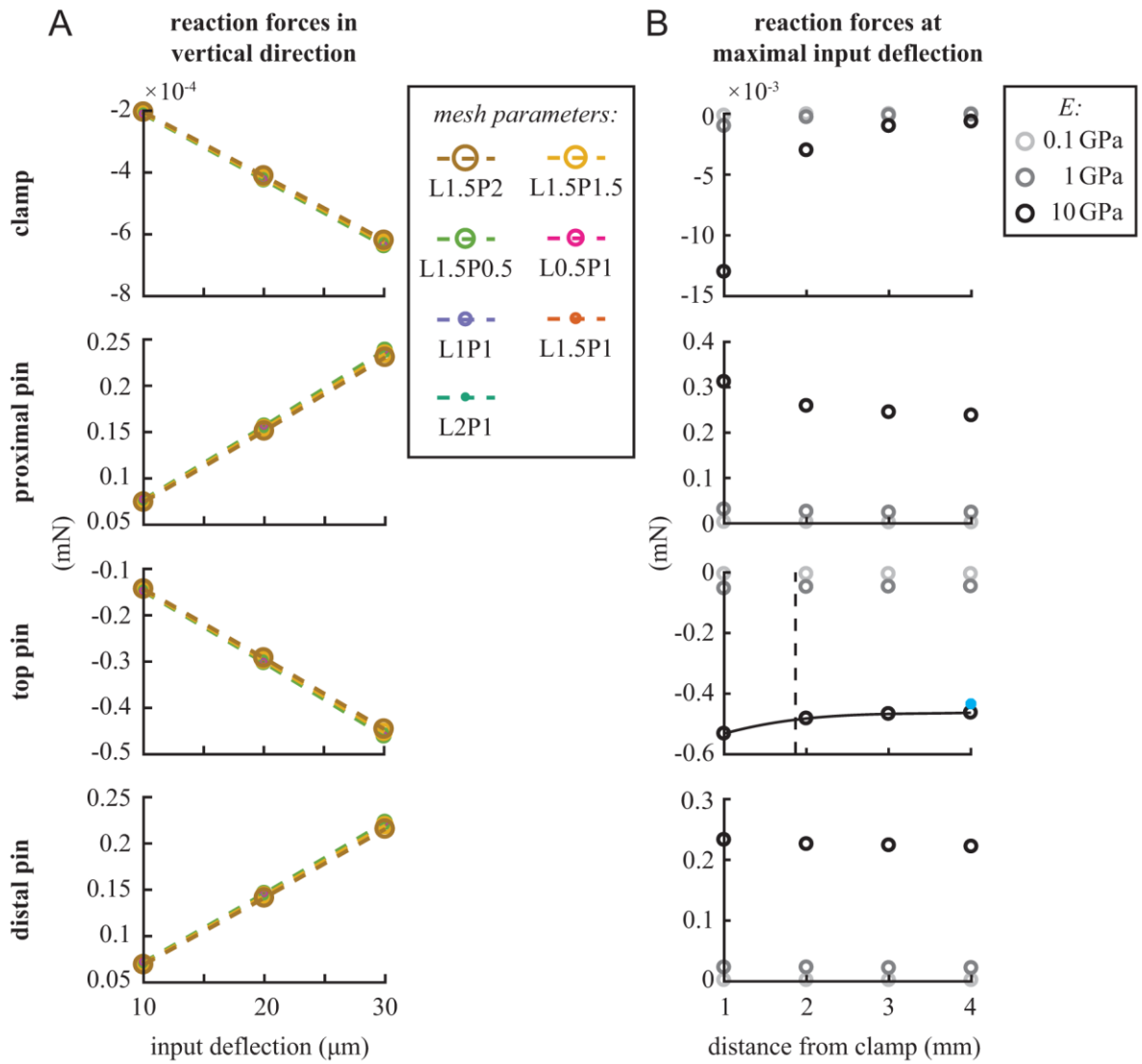

Fig 6. FEM computed reaction forces in the vertical direction during deflections at the clamped end of the beam and the three pins. A) Reaction forces during all three input deflections. Several simulations at x=4 mm were performed while varying the mesh density both along the length and the perimeter of the beam. The seed sizes are indicated in the legend; for example, L2P1 indicates 2 µm grid along the length of the beam and 1 µm mesh along its perimeter. The mesh density has a negligible effect on the reaction forces. Final simulations were therefore performed with the mesh grid size of 1 µm. **B)** Vertical force during maximal deflection (30 µm). Shades of grey correspond to different beam stiffnesses (*E*; darker colours indicate stiffer beams); the light blue circle in the graph with the results for the top pin indicates the bent-beam (*E*=10 GPa) simulation. Clamping has little effect when the Young's modulus (*E*) of the beam is smaller or equal to 1 GPa. In stiffer cantilever beams (*E*=10 GPa), the recorded forces increase with the vicinity of the clamp. The

data for the top pin was interpolated using a cubic spline (black line) to calculate the reliability threshold for the force measurements. The threshold was set to the force difference of 5% or more compared to the output at 4 mm (black, vertical, dashed line).

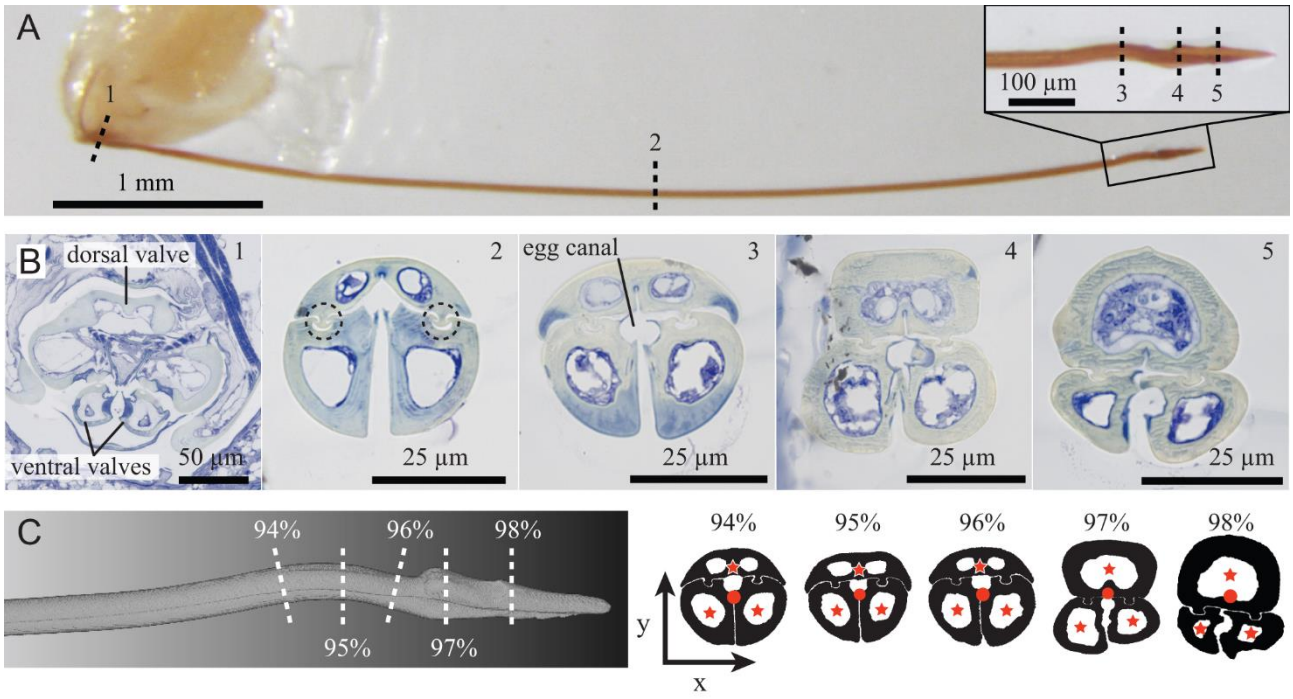

Fig 7. Gross anatomy of the ovipositor. A) Lateral view of a dissected ovipositor of *D. longicaudata* with parts of its basal plates that are involved in actuation (left side). Dorsal valve is on the top, ventral valves on the bottom. Inset - close up of the distinct tip morphology: the S-bend region (3) and the bulge of the dorsal valve (4). **B)** Histological cross-sections of the ovipositor at locations shown in A, stained for proteins (blue). Dorsal side is up. The tongue-and-groove mechanism is indicated with black, dashed circles in (2). **C)** 3D reconstruction of the high-resolution µCT scan of the ovipositor tip with minimal cross-sections calculated at indicated locations. The dorsal side is up. The centroids used in calculations of the second moments of area (in Cartesian coordinate system x, y) are indicated in the cross-sections: red dots for whole ovipositor, red stars for individual valves.

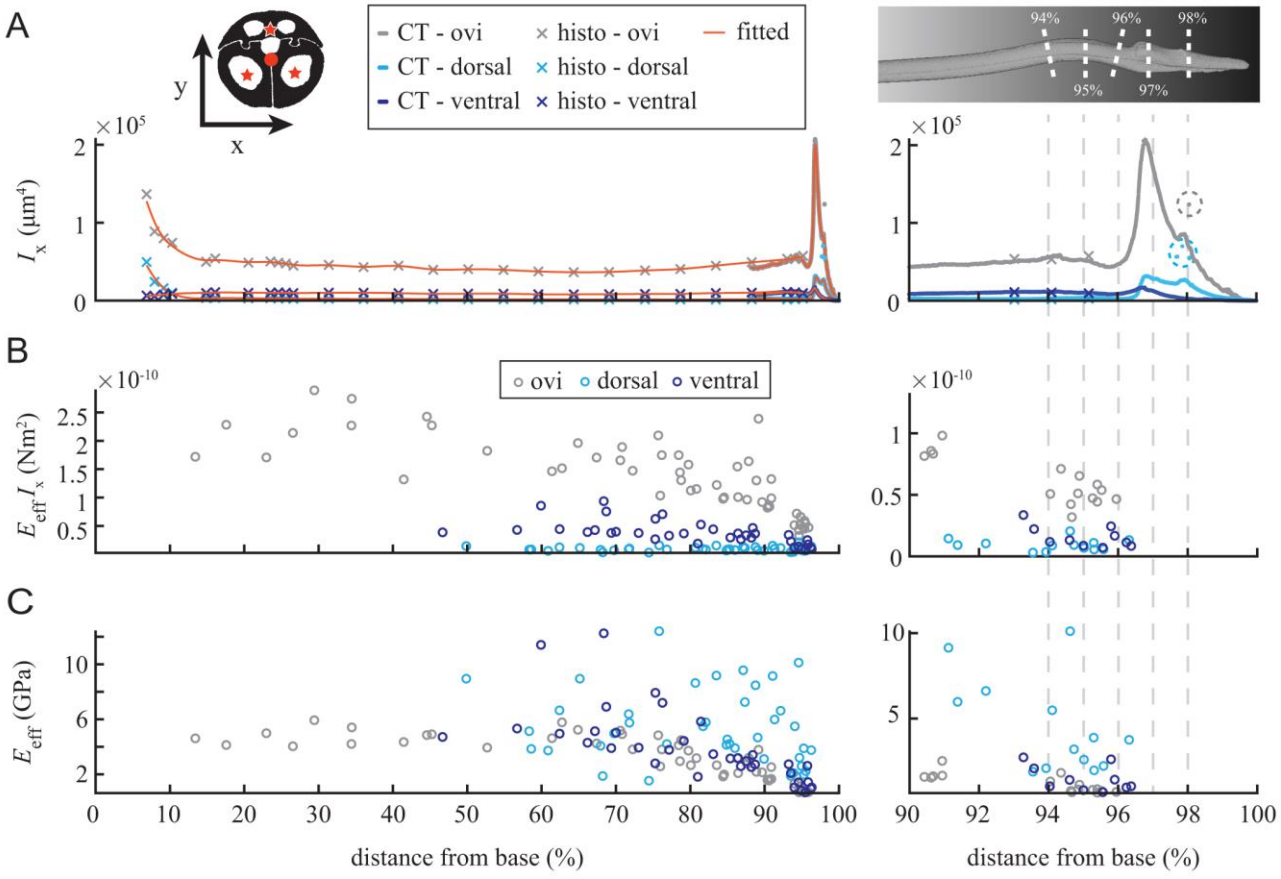

Fig 8. Ovipositor geometry, bending stiffness, and effective modulus of elasticity vary along its length. Left: values along most of the ovipositor length; right: a close up of the distal region of the ovipositors. **A)** The second moment of area around the x-axis (I_x) changes little along most of the ovipositor length. Grey: whole ovipositor; dark blue: ventral valve (mean of both elements); light blue: dorsal valve; orange lines: fitted cubic smoothing spline (smoothing parameters 0.98 and 0.5 were used for the µCT and histological data, respectively). Crosses: histological data; thick curves (>88% from base) are actually overlapping dots of µCT data, with the verified erroneous artefacts resulting from the recalculation of the minimal cross-sectional area indicated in dashed circles of corresponding colours. The two types of data were scaled and then combined (see SI). **B)** Bending stiffness ($E_{eff}\ I_x$) of the ovipositor and the ventral valves decreases in the distal direction and is lowest in the pre-bent S-shaped region. The $E_{eff}\ I_x$ of the dorsal valve varies little along its length. Combined data of 23 samples. **C)** The effective material stiffness (E_{eff}) of the whole ovipositor and individual valves is smaller in the S-bend region than in the rest of the ovipositor. Combined data of 23 samples.

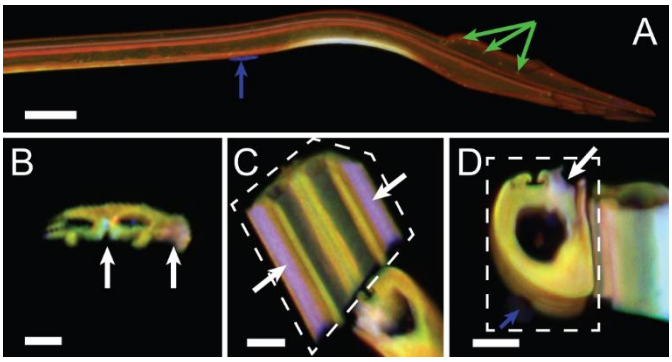

Fig 9. Qualitative analysis of material composition of insect cuticle using its autofluorescent properties. The blue channel (405 nm excitation) indicates resilin. The green (488 nm excitation) and red channel (555 and 639 nm excitation) indicate well sclerotized cuticle. Blue arrows mark dirt on the surface of the ovipositor. **A)** The distal part of the ovipositor showing high resilin presence in the ventral part of the S-shaped region—top: dorsal valve; bottom: ventral valve (see also **Fig S3**). Green dots are most likely sensors (green arrows). **B)** Cross-section of the dorsal valve from the S-shaped region showing resilin near the egg canal (central white arrow) and in the lateral edge (right white arrow). **C)** Ventral view of the dorsal valve (top, surrounded by a white, dashed line) showing resilin-rich regions along its lateral side (white arrows) and one of the ventral valves in cross-section (bottom right). The CLSM scan was optimized for the dorsal valve and the colours of the ventral valve may not be representative of its material composition. **D)** Cross-section through the ventral valve proximal to the S-shaped region (left, surrounded by a white, dashed line) showing resilin presence in the wall of the egg canal (white arrow) and lateral view of another ventral valve (right). The CLSM scan was optimized for the cross-sectional view and the colours of the side view might not be representative of the material composition of that part. Scale bars: 50 µm (A), 10 µm (B–D).

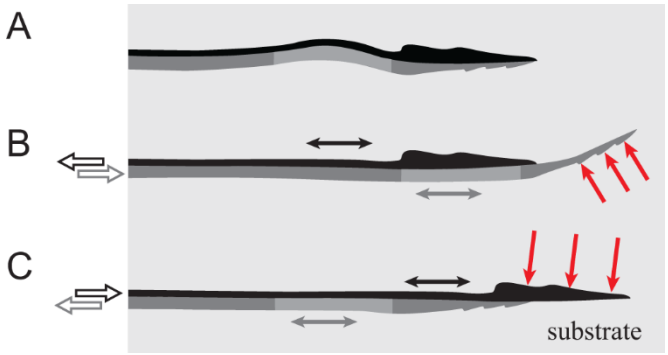

Fig 10. Proposed steering mechanism in *D. longicaudata*. **A)** Ovipositor with aligned valves (black: dorsal; dark grey: ventral) shows a straight shaft, the adjacent S-shaped region, and the tip. **B)** Protraction of the ventral valves (movement indicated by open arrows) presumably straightens the less rigid S-shaped region (light grey section) as it aligns with the stiff tip of the dorsal valve, which results in dorsal curving of the ventral valve tips. We hypothesize that the bending of the ventral valves is enhanced by the asymmetrical substrate forces acting on the bevelled tip (red arrows). **C)** Protraction of the dorsal valve presumably straightens its S-shaped region as it aligns with the ventral valve tips. The S-shaped region of the ventral valves is probably also straightened which might potentially lead to dorsal curving. However, we hypothesize that the bevelled tip of the dorsal valve induces asymmetric reaction forces from the substrate that counteract these bending moments and thus a straight protraction is observed.

Supplementary Information

1. Figures

Force transducer characteristics

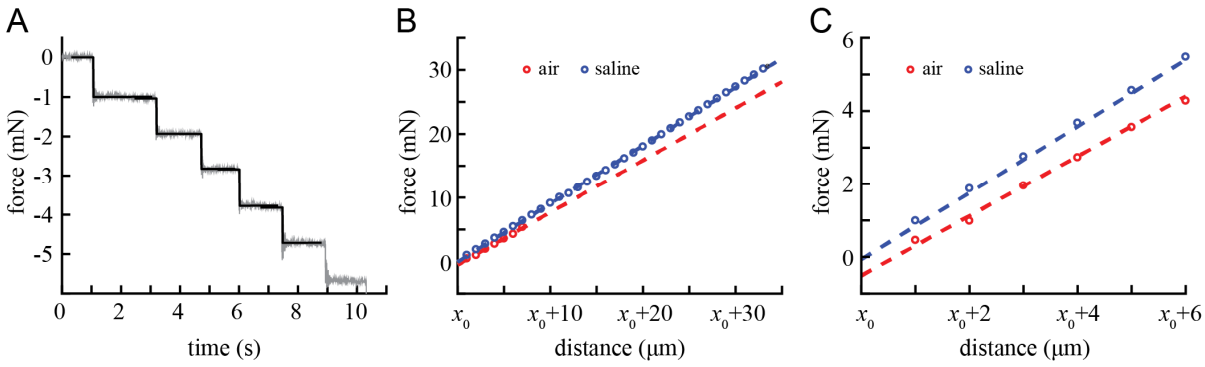

Fig S1. Linearity of the force transducer measurements. A) Raw data (grey) with superimposed fits (black) of two perpendicular razorblades pressed against each other. **B)** Force-deflection graphs for measurements in air (red) and saline (blue). The vertical offset between the curves is due to the difference in initial conditions (i.e. the vicinity of the razor blades before the step in which contact was made). **C)** First six deflection steps from the graphs shown in B. The dynamic range of the force transducer used in the experiments is 0–10 g, with a resolution of <1 mg (= 0.01 mN).

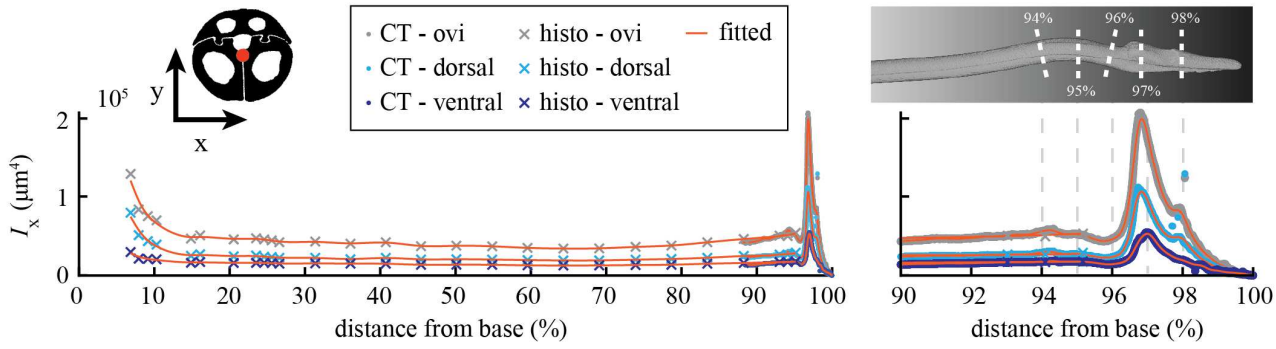

Fig S2. Contribution to the ovipositor second moment by individual valves. I_x values for the valves are higher than in **Fig 8A** because we used the centroid of the whole ovipositor (red dot in the schematics) in all calculations. The dorsal valve contributes more to the ovipositor second moment of area than each individual ventral valve, because compared to the ventral valves, a greater part of the dorsal valve is located further away from the ovipositor centroid.

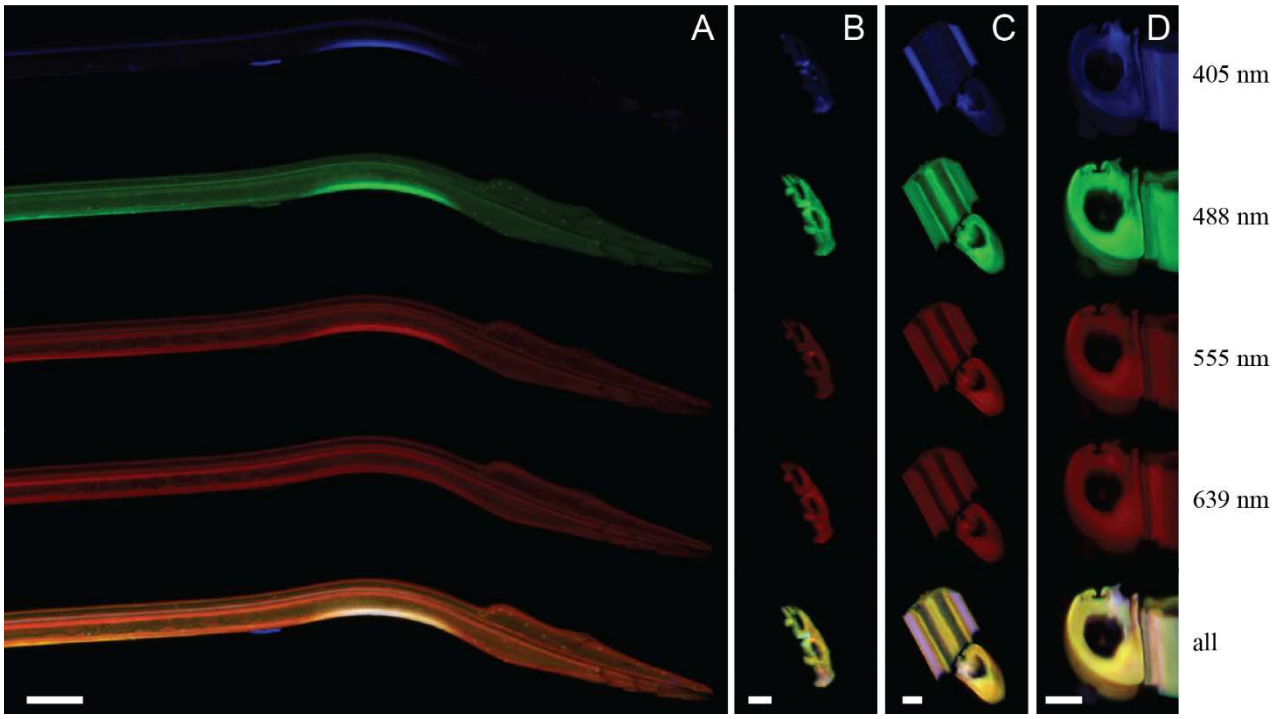

Fig S3. Autofluorescences (split in different channels) recorded from the ovipositor. Autofluorescence of materials excited with different wavelengths shows gradients in material composition in the distal part of the ovipositor. Excitation wavelengths indicated in the figure on the right. **A)** Distal part of the ovipositor. **B, C, D)** Sections from the distal region of the ovipositor, but proximal to its S-shaped region. (**B**) Dorsal valve cross-section (**C**) Dorsal valve inner side and ventral valve cross-section. The scan was optimized for the dorsal valve and the colours of the ventral valve might not be representative of its material composition. (**D**) Ventral valve cross section and side view. The scan was optimized for the cross-sectional view, so the colours of the side view do not reflect the material composition of the valve. Scale bars: 50 µm (**A**), 10 µm (**B–D**).

2. Tables

Table S1. Mean Second Moment of Area of regions of fitted data based on CT-scans only. For centroids see Fig 3. The shaft, S-region and tip are for each structure significantly different (Mann-Whitney *U* test, P<0.05). The bulge is defined as the part of the tip where I_x is larger than the mean I_x of the shaft.

	Second Moment of Area (I_x, µm^4 1 × 10^4)			
	Shaft <93% OL	S-Region 93-96% OL	Tip-region >96% OL	Bulge
Dorsal valve	0.25 ± 0.02 max=0.27 (n=1655)	0.30 ± 0.06 max=0.39 (n=999)	1.27 ± 1.05 max=3.06 (n=1227)	96.29–99.41 %OL Mean = 1.60 ± 0.97 (n=941)
Ventral valve	0.94 ± 0.10 max=1.13 (n=1555)	1.06 ± 0.10 max=1.16 (n=1001)	0.55 ± 0.54 max=1.61 (n=1229)	96.14–97.21 %OL Mean = 1.30 ± 0.22 (n=347)
Whole ovipositor	4.51 ± 0.28 max=5.04 (n=1665)	5.13 ± 0.39 max=5.74 (n=1018)	7.31 ± 5.78 Max=19.93 (n=1208)	95.99–98.34 %OL Mean = 10.21 ± 4.82 (n=769)

Table S2. Measured bending stiffness and calculated effective modulus of elasticity of the shaft and S-region of ovipositors, dorsal and ventral valves. Diff. indicates the significance level of the difference between the shaft and S-region for the specific parameter obtained with a Mann-Whitney *U* test. When comparing values within each column, only the E_{eff} of the shaft of the ventral valve and the whole ovipositor do not significantly differ (Mann-Whitney *U* test, P=N.S.).

	Bending stiffness ($E_{eff}I_x$, 1 × 10^{-11} Nm^2)				Effective modulus of elasticity (E_{eff}, GPa)		
	Shaft <93% OL	S-Region 93-96% OL	Diff.		Shaft <93% OL	S-Region 93-96% OL	Diff.
Dorsal valve	0.90 ± 0.33 (n=30)	0.88 ± 0.52 (n=10)	P=N.S.		5.95 ± 2.53 (n=30)	3.70 ± 2.51 (n=10)	P<0.01
Ventral valve	4.40 ± 1.85 (n=26)	1.57 ± 0.85 (n=10)	P<0.001	P=N.S.	4.81 ± 2.56 (n=26)	1.46 ± 0.74 (n=10)	P<0.001
Whole ovipositor	15.72 ± 5.37 (n=42)	5.12 ± 1.09 (n=11)	P<0.001		3.60 ± 1.27 (n=42)	0.92 ± 0.35 (n=11)	P<0.001

3. **Videos**

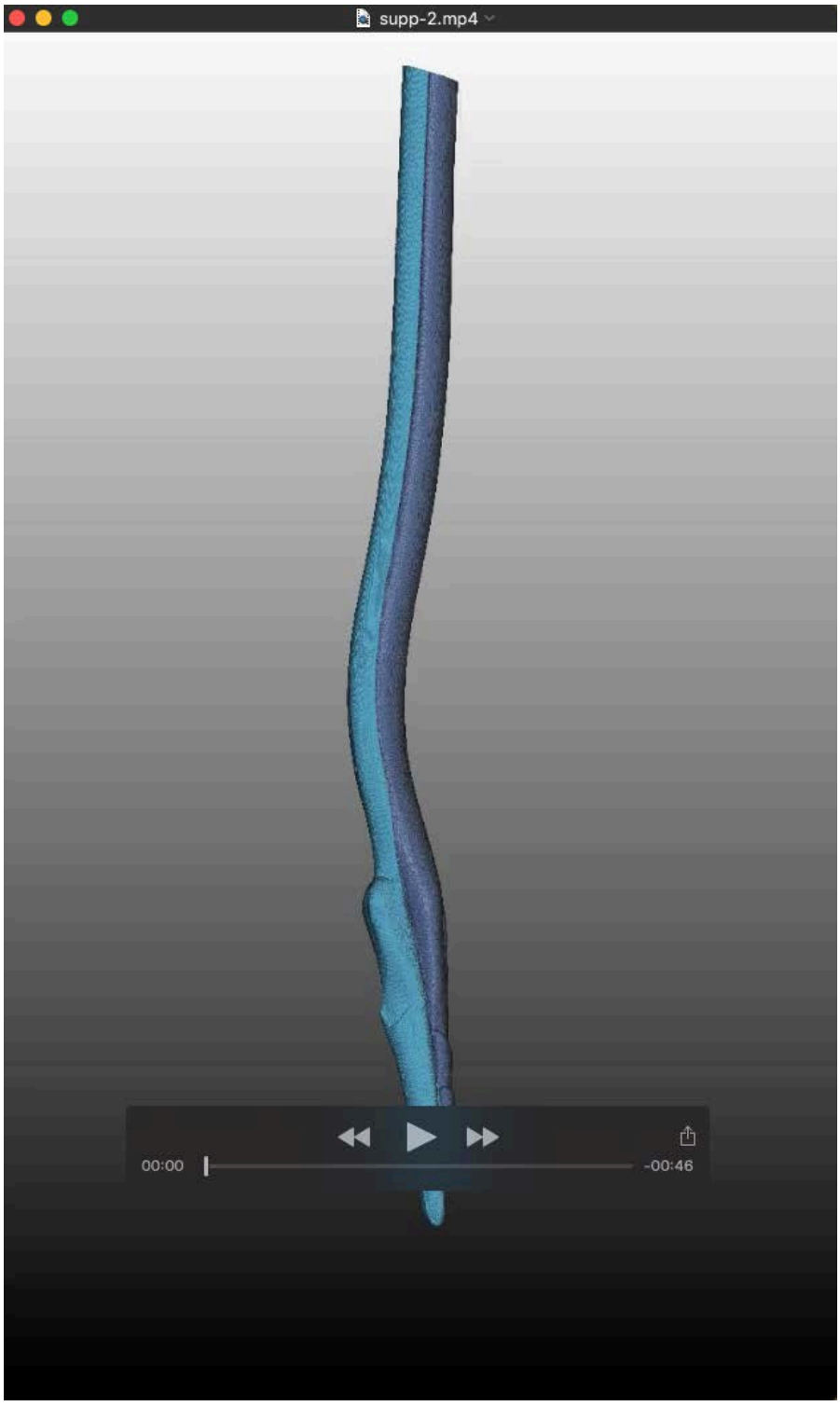

Movie 1. Segmented µCT scan of the ovipositor. Colour code same as in graphs (**Fig 3**); dorsal valve is light blue and ventral valves are dark blue. The characteristic S-shaped region of the ovipositor, the bevel shaped tips, the widening of the dorsal valve, and the serrations on the ventral valves are clearly visible. Additionally, tongue-and-groove mechanisms on the inner sides of the ovipositor are straight and do not show morphological variations.

Movie 2. Curved and straight ovipositor insertions in the substrate. Protraction of ventral valve(s) within the substrate leads to dorsal curving of the ovipositor's distal end. In contrast, protraction of the dorsal valve within the substrate does not lead to noticeable curving of the ovipositor, which therefore makes a straight path. Videos obtained as described in Cerkvenik et al. (2017). Videos show insertion in 2% gelatine, slowed down approximately 10x.

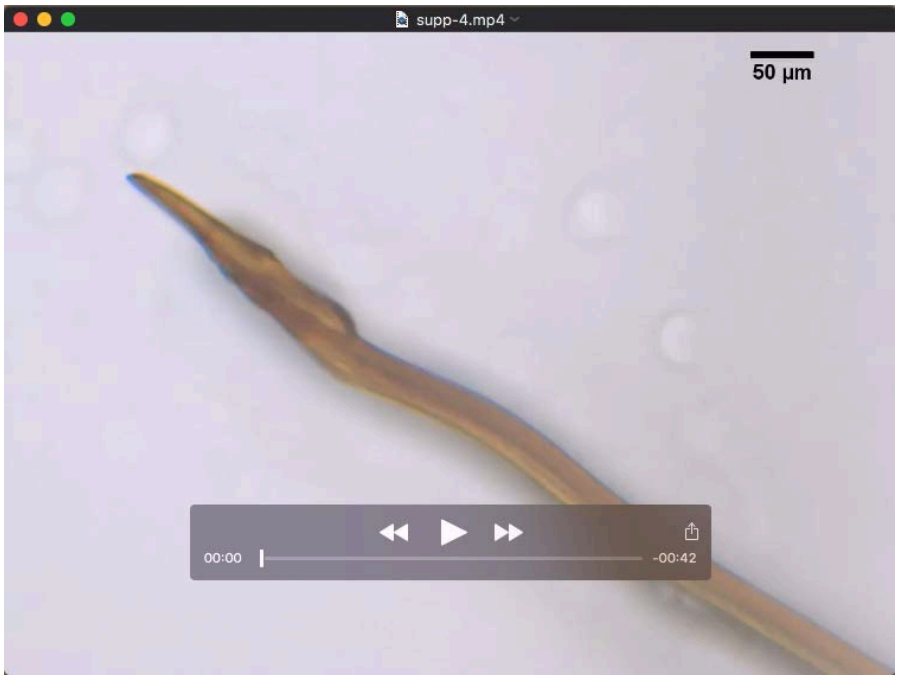

Movie 3. Valve movements outside the substrate. Spontaneous valve movements outside the substrate observed under microscope—the animal was **not** in the probing position and a cover glass was put on top of the ovipositor to keep it in the focal plane. Protraction of both the dorsal and the ventral valves causes dorsal curving of the ovipositor distal end. Video recorded with Leica DFC 450 C camera (5 MP) mounted on Leica DM6b microscope (Leica Microsystems). Slowed down approximately 4x.

Supplementary Information

1. Figures

Force transducer characteristics

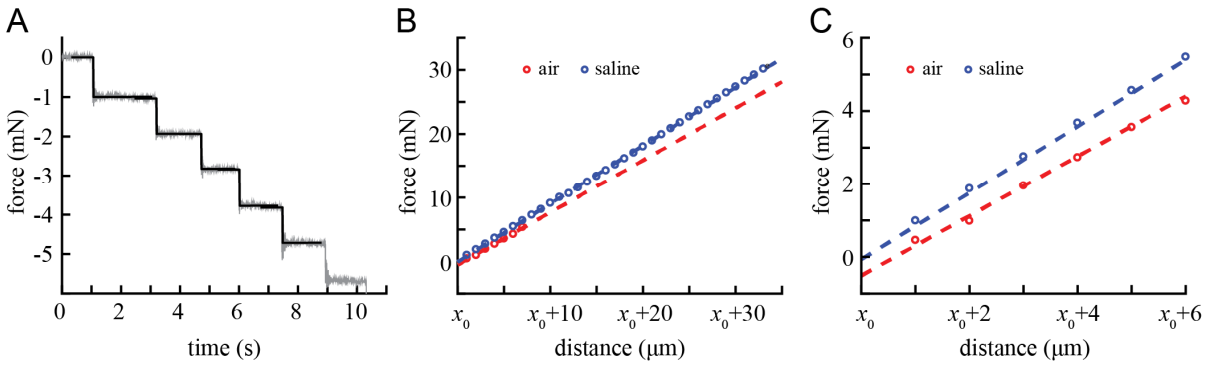

Fig S1. Linearity of the force transducer measurements. A) Raw data (grey) with superimposed fits (black) of two perpendicular razorblades pressed against each other. **B)** Force-deflection graphs for measurements in air (red) and saline (blue). The vertical offset between the curves is due to the difference in initial conditions (i.e. the vicinity of the razor blades before the step in which contact was made). **C)** First six deflection steps from the graphs shown in B. The dynamic range of the force transducer used in the experiments is 0–10 g, with a resolution of <1 mg (= 0.01 mN).

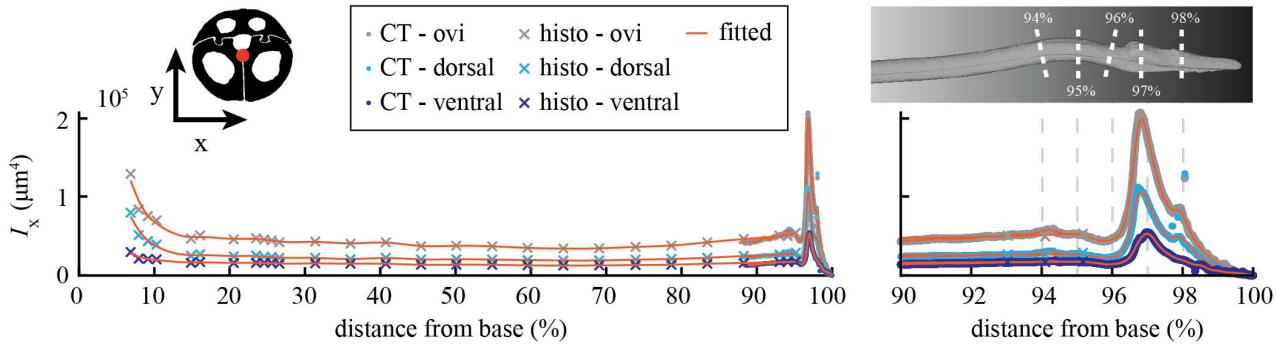

Fig S2. Contribution to the ovipositor second moment by individual valves. I_x values for the valves are higher than in **Fig 8A** because we used the centroid of the whole ovipositor (red dot in the schematics) in all calculations. The dorsal valve contributes more to the ovipositor second moment of area than each individual ventral valve, because compared to the ventral valves, a greater part of the dorsal valve is located further away from the ovipositor centroid.

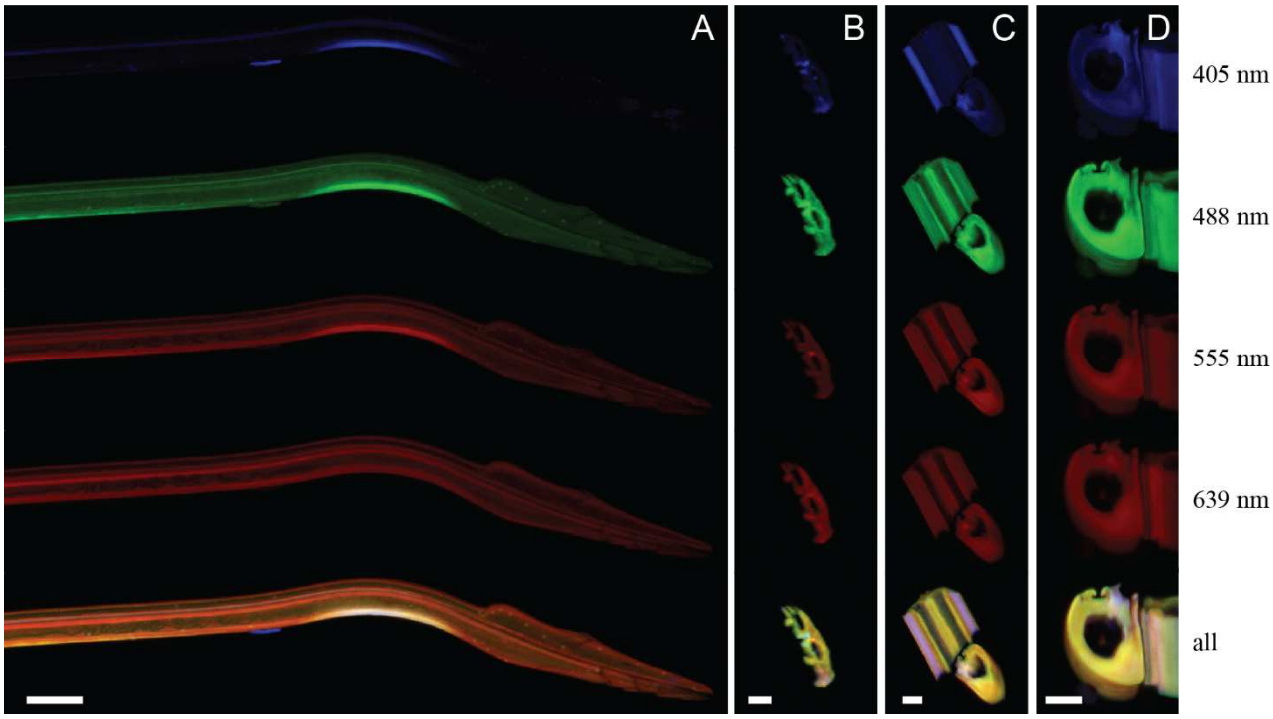

Fig S3. Autofluorescences (split in different channels) recorded from the ovipositor. Autofluorescence of materials excited with different wavelengths shows gradients in material composition in the distal part of the ovipositor. Excitation wavelengths indicated in the figure on the right. **A)** Distal part of the ovipositor. **B, C, D)** Sections from the distal region of the ovipositor, but proximal to its S-shaped region. (**B**) Dorsal valve cross-section (**C**) Dorsal valve inner side and ventral valve cross-section. The scan was optimized for the dorsal valve and the colours of the ventral valve might not be representative of its material composition. (**D**) Ventral valve cross section and side view. The scan was optimized for the cross-sectional view, so the colours of the side view do not reflect the material composition of the valve. Scale bars: 50 µm (**A**), 10 µm (**B–D**).

2. Tables

Table S1. Mean Second Moment of Area of regions of fitted data based on CT-scans only. For centroids see Fig 3. The shaft, S-region and tip are for each structure significantly different (Mann-Whitney *U* test, P<0.05). The bulge is defined as the part of the tip where I_x is larger than the mean I_x of the shaft.

	Second Moment of Area (I_x, µm^4 1 × 10^4)			
	Shaft <93% OL	S-Region 93-96% OL	Tip-region >96% OL	Bulge
Dorsal valve	0.25 ± 0.02 max=0.27 (n=1655)	0.30 ± 0.06 max=0.39 (n=999)	1.27 ± 1.05 max=3.06 (n=1227)	96.29–99.41 %OL Mean = 1.60 ± 0.97 (n=941)
Ventral valve	0.94 ± 0.10 max=1.13 (n=1555)	1.06 ± 0.10 max=1.16 (n=1001)	0.55 ± 0.54 max=1.61 (n=1229)	96.14–97.21 %OL Mean = 1.30 ± 0.22 (n=347)
Whole ovipositor	4.51 ± 0.28 max=5.04 (n=1665)	5.13 ± 0.39 max=5.74 (n=1018)	7.31 ± 5.78 Max=19.93 (n=1208)	95.99–98.34 %OL Mean = 10.21 ± 4.82 (n=769)

Table S2. Measured bending stiffness and calculated effective modulus of elasticity of the shaft and S-region of ovipositors, dorsal and ventral valves. Diff. indicates the significance level of the difference between the shaft and S-region for the specific parameter obtained with a Mann-Whitney *U* test. When comparing values within each column, only the E_{eff} of the shaft of the ventral valve and the whole ovipositor do not significantly differ (Mann-Whitney *U* test, P=N.S.).

	Bending stiffness ($E_{eff}I_x$, 1 × 10^{-11} Nm^2)				Effective modulus of elasticity (E_{eff}, GPa)		
	Shaft <93% OL	S-Region 93-96% OL	Diff.		Shaft <93% OL	S-Region 93-96% OL	Diff.
Dorsal valve	0.90 ± 0.33 (n=30)	0.88 ± 0.52 (n=10)	P=N.S.		5.95 ± 2.53 (n=30)	3.70 ± 2.51 (n=10)	P<0.01
Ventral valve	4.40 ± 1.85 (n=26)	1.57 ± 0.85 (n=10)	P<0.001	P=N.S.	4.81 ± 2.56 (n=26)	1.46 ± 0.74 (n=10)	P<0.001
Whole ovipositor	15.72 ± 5.37 (n=42)	5.12 ± 1.09 (n=11)	P<0.001		3.60 ± 1.27 (n=42)	0.92 ± 0.35 (n=11)	P<0.001

3. **Movies**

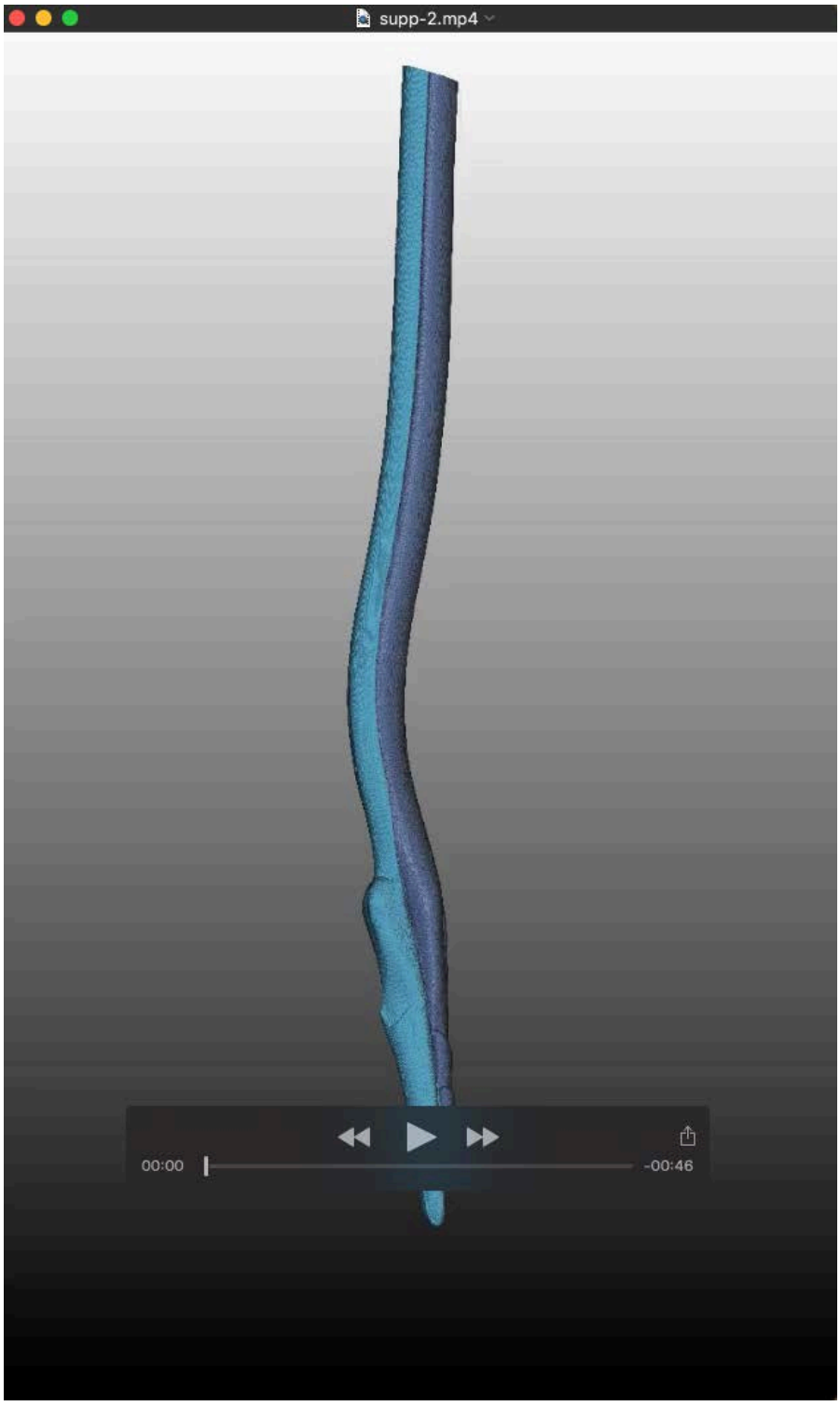

Movie 1. Segmented µCT scan of the ovipositor. Colour code same as in graphs (**Fig 3**); dorsal valve is light blue and ventral valves are dark blue. The characteristic S-shaped region of the ovipositor, the bevel shaped tips, the widening of the dorsal valve, and the serrations on the ventral valves are clearly visible. Additionally, tongue-and-groove mechanisms on the inner sides of the ovipositor are straight and do not show morphological variations.

Movie 2. Curved and straight ovipositor insertions in the substrate. Protraction of ventral valve(s) within the substrate leads to dorsal curving of the ovipositor's distal end. In contrast, protraction of the dorsal valve within the substrate does not lead to noticeable curving of the ovipositor, which therefore makes a straight path. Videos obtained as described in Cerkvenik et al. (2017). Videos show insertion in 2% gelatine, slowed down approximately 10x.

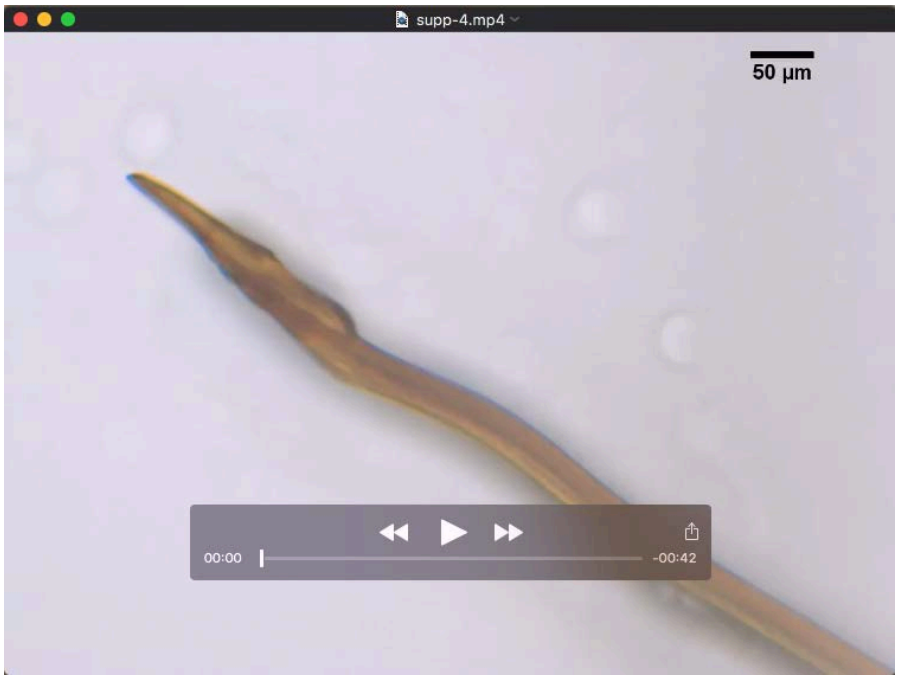

Movie 3. Valve movements outside the substrate. Spontaneous valve movements outside the substrate observed under microscope—the animal was **not** in the probing position and a cover glass was put on top of the ovipositor to keep it in the focal plane. Protraction of both the dorsal and the ventral valves causes dorsal curving of the ovipositor distal end. Video recorded with Leica DFC 450 C camera (5 MP) mounted on Leica DM6b microscope (Leica Microsystems). Slowed down approximately 4x.